Cite as: B. D. Cosgrove et al., Science 10.1126/science.adl1988 (2025).

Mechanosensitive genomic enhancers potentiate the cellular response to matrix stiffness

Brian D. Cosgrove^{1,2+}, Lexi R. Bounds^{1,2+}, Carson Key Taylor^{1,2+}, Alan L. Su^{1,2}, Anthony J. Rizzo^{1,2}, Alejandro Barrera^{2,3}, Tongyu Sun⁴, Alexias Safi^{2,5}, Lingyun Song^{2,5}, Thomas Whitlow⁴, Aleksandra Tata^{4,6}, Nahid Iglesias^{1,2}, Yarui Diao^{2,4,7}, Purushothama Rao Tata^{2,4,7,8}, Brenton D. Hoffman^{1,4*}, Gregory E. Crawford^{2,5*}, Charles A. Gersbach^{1,2,4,6,7}*

1Department of Biomedical Engineering, Duke University, Durham, NC, USA. 2Center for Advanced Genomic Technologies, Duke University, Durham, NC, USA. 3Department of Biostatistics and Bioinformatics, Duke University, Durham, NC, USA. Department of Cell Biology, Duke University, Durham, NC, USA. Department of Pediatrics, Duke University Medical Center, Durham, NC, USA. Department of Surgery, Duke University Medical Center, Durham, NC, USA. Duke Regeneration Center, Duke University, Durham, NC, USA. 8Division of Pulmonary, Allergy, and Critical Care Medicine, Department of Medicine, Duke University School of Medicine, Durham, NC, USA.

*Corresponding author. Email: charles.gersbach@duke.edu (C.A.G.); greg.crawford@duke.edu (G.E.C.); brenton.hoffman@duke.edu (B.D.H.)

†These authors contributed equally to this work.

Epigenetic control of gene expression and cellular phenotype is influenced by changes in the local microenvironment, yet how mechanical cues precisely influence epigenetic state to regulate transcription remains largely unmapped. Here, we combine genome-wide epigenome profiling, epigenome editing, and phenotypic and single-cell RNA-seq CRISPR screening to identify a class of genomic enhancers that responds to the mechanical microenvironment. These "mechanoenhancers" can be preferentially activated on either soft or stiff extracellular matrix contexts and regulate transcription to influence critical cell functions including apoptosis, adhesion, proliferation, and migration. Epigenetic editing of mechanoenhancers reprograms the cellular response to the mechanical microenvironment and modulates the activation of disease-related genes in lung fibroblasts from healthy and fibrotic donors. Epigenetic editing of mechanoenhancers holds potential for precise targeting of mechanically-driven diseases.

The cellular microenvironment is a potent regulator of cellular behavior (1, 2). Advances in epigenetic profiling and CRISPR screening have deepened our understanding of how chemical stimuli including hormones, cytokines, and pharmacologic interventions shape the epigenetic landscape (3-6). Mechanical stimuli from the microenvironment, such as stiffness of the extracellular matrix (ECM) or applied forces, are also potent regulators of many fundamental cell processes, including growth, death, differentiation, and migration, and play keys roles in tissue development, regeneration, aging, and disease pathology such as fibrosis, tumor formation, and atherosclerosis (7-10). Mechanosensitive gene regulation occurs across a variety of pathways through nucleo-cytoplasmic shuttling of transcriptional co-regulators (11), including YAP and MRTF (12-14). These proteins shuttle to the nucleus through pathways responsive to mechanical cues, such as nuclear pore deformation (15) and F/G-actin ratios (16-18). Mechanical force has additionally been shown to modulate epigenetic modifications (19-22) and directly deform chromatin (23, 24), both of which can influence patterns of gene expression.

Traditionally, the binding of transcription factors and coactivators at promoter regions has been the classical mechanism for modulation of target gene expression. However, genome annotation efforts over the last two decades have described the critical role of non-coding gene regulatory regions that occur predominantly outside promoters (25). For instance, the mechanosensitive co-activators YAP/TAZ can bind to distal enhancers in cells cultured on rigid tissue culture plastic (26, 27). Enhancers act across variable genomic distances to regulate transcription and are marked by a combination of chromatin accessibility, presence of active histone marks (e.g., H3K27ac), depletion of repressive histone marks (e.g., H3K9me3), transcription factor binding, and chromatin looping to distal target genes (28). The complex logic of gene regulation by these distal elements has been notoriously difficult to dissect, but advances in high-throughput CRISPR screening and single-cell genomics have transformed the capability to classify how and where these cis-regulatory elements modulate transcription across the genome (4, 5, 29, 30).

Despite these recent developments, the impact of mechanical stimuli on the non-coding genome and the resulting transcriptional and phenotypic responses remain largely unmapped. Here, we utilized genome-wide chromatin accessibility profiling, epigenetic editing, high-throughput CRISPR screening, and single-cell sequencing to characterize how ECM stiffness cues activate cis-regulatory elements to regulate gene expression. Through this work we identify and validate a novel set of cis-regulatory elements that are responsive to changes in the mechanical microenvironment. For simplicity, we term these regions as "mechanoenhancers" and show they behave as key drivers for downstream mechanically-driven behaviors in human cells. This work provides new insights into the regulation of gene expression by mechanical cues.

Results

Widespread changes in gene expression and chromatin accessibility result from short-term exposure to physiologically soft or stiff substrates

We first characterized the response of gene expression and chromatin structure to changes in ECM stiffness cues by culturing primary human neonatal foreskin fibroblasts (HFF cells) and A549 tumor-derived lung epithelial cells on substrate stiffness conditions mimicking a range of pericellular environments found in both healthy and diseased tissues. Fibroblasts were chosen due to their key role in ECM synthesis and their contribution to tissue fibrosis (31), and have been extensively profiled via functional genomics. Similarly, the A549 cell line responds to ECM stiffness (32), complements skin fibroblasts, and has extensive functional genomics data readily available (33-35). Cells were cultured for 20 hours on either soft (elastic modulus, E = 1 kPa, mimicking soft connective tissues) or stiff (E= 50 kPa, mimicking organized musculoskeletal tissues or fibrotic lesions) polyacrylamide hydrogels (9, 36, 37), as well as on tissue culture plastic (TCP, E= ~1 GPa). The 20-hour time point minimizes transcriptional feedback that could further complicate understanding the direct influence of ECM stiffness on epigenetic state. After 20 hours, cells were harvested to examine both transcriptional changes (RNA-seq) and chromatin accessibility changes (ATAC-seq) in response to these ECM stiffness cues (Fig. 1A). We performed all sequencing experiments in at least duplicate per condition, and all RNA-seq and ATAC-seq data were highly reproducible and met appropriate quality control metrics (fig. S1 and table S1).

Transcriptomic analysis identified 4,009 differentially expressed genes in HFFs and 221 differentially expressed genes in A549 cells (defined as false discovery rate (FDR) < 0.05 and absolute value(log₂[Fold-Change]) > 0.5) (Fig. 1, B and C, and tables S2 and S3). The disparity in the number of differentially expressed genes between the two cell types may reflect the difference in mechanical memory between primary cells and immortalized lines, with transcriptional adaptation potentially occurring after longer subculturing and increased mechanical memory in A549 cells (38). Notably, 76 genes were differentially expressed in both cell types, including canonical genes associated with YAP/TAZ translocation (CYR61, CTGF, AMOTL2, ANKRD1, and NUAK2) up-

First release: 25 September 2025

regulated on stiffer materials (Fig. 1D), consistent with previous studies (39, 40).

We next compared changes in chromatin accessibility between the soft and stiff hydrogels by ATAC-seq. After 20 hours of culture, we observed widespread changes in chromatin accessibility in both cell types, with ~23% of identified accessible chromatin peaks showing significant (FDR < 0.01, abs(Log2 Fold-Change)>1) differential accessibility in HFF cells and ~15% in A549 cells between the two materials (Fig. 1, E and F, and tables S4 and S5). In both cell types, there was an equal distribution of peaks exhibiting increased accessibility on soft and stiff conditions. Both cell types shared only about 10% of peaks that were more accessible on soft hydrogels (N=1,071 peaks) or stiff hydrogels (N=4,522 peaks) (Fig. 1G). The main difference between substrate conditions was that more promoters were accessible on 50 kPa hydrogels (fig. S2). This highlights that while these regions are sometimes shared between cell types, the vast majority of these regions were cell type-specific (Fig. 1, H and I), in accordance with previous observations of cell type specificity of genomic enhancers (41). We then investigated the short-term reversibility of changes in chromatin accessibility in response to small molecule inhibitors of intracellular acto-myosin contractility (Y-27632) and key co-activator protein-protein interactions, verteporfin (TEAD-YAP interaction) and CCG-222740 (MRTF-A/CArG) (42, 43) (supplementary text 1, figs. S5 and S6, and tables S6 and S31). HFFs cultured on 50 kPa hydrogels had 7,131 differentially accessible peaks after one hour treatment with Y-27632. Treatment with verteporfin and CCG-222740 for 18 hours resulted in similar magnitude changes in differentially accessible peaks, with newly closed peaks being enriched for TEAD and CArG/SRF motifs for each inhibitor, respectively. These results highlight the role of mechanical force and mechanosensitive signaling in altering the accessible chromatin landscape.

To further identify transcription factor modules that might be driving these accessibility changes, we performed de novo transcription factor motif analysis on the differentially accessible peaks for both material conditions and cell types, revealing enrichment for ATF, FOXF1, and CEBPA on soft hydrogels and TEAD, FOXA, HNF1B, and LEF motifs on stiff hydrogels (fig. S3). We additionally performed TOBIAS transcription factor footprinting analyses on the ATAC-seq data (44) to determine if there were stiffness-mediated changes in protein-DNA engagement within these differentially accessible chromatin peaks across material stiffness conditions. Footprinting analysis showed more protein engagement around TEAD family motifs on 50 kPa hydrogels in HFF and A549 cells, and at HNF1 motifs in A549 cells on 50 kPa (Fig. 1, J and K; fig. S4; and tables S24 and S25). The enrichment of TEAD on stiff materials is consistent with the known role **TEAD** YAP/TAZ-mediated of in

mechanotransduction (26, 45–47). On soft 1 kPa hydrogels, CEBP family motifs and ZBTB motifs were the most preferentially bound in HFF and A549 cells, respectively (Fig. 1, J and K). Other motif families with differential engagement across 1 and 50 kPa hydrogels in both HFF and A549 cells included JUN/FOS (AP1), ATF, and ELK. In summary, both motif analysis and transcription factor footprinting identify TEAD, HNF, and CEBP as being the most differentially engaged transcription factor families across materials of differential stiffness in HFF and A549 cells.

Previous work suggests chromatin looping can facilitate interactions between cis-regulatory elements and the genes they regulate. To investigate if mechanical stimuli altered 3-D chromatin interactions, we performed HiCAR (Hi-C on accessible regulatory DNA) on HFF cells cultured on either soft (1 kPa) or stiff (50 kPa) hydrogels. Of the called loops (tables S7 and S8), ~12.5-12.8% were unique to a given stiffness condition, whereas ~43.5-46.7% of called loops had overlapping loop anchors for both materials (fig. S7, A and B). We next compared the chromatin loops and the differentially accessible ATAC-seq peaks for each ECM stiffness condition, and 42.4%-42.9% of chromatin loop anchors overlapped at least one differentially accessible ATAC-seq peak. For both soft and stiff hydrogels, a larger proportion of ATAC-seq peaks that overlap loop anchors were substantially more accessible in the ECM stiffness condition for which the loop was called (fig. S7C). Specifically, 51.2% of differentially accessible ATAC-seq peaks that overlapped a chromatin loop in cells cultured on soft hydrogels were more accessible on soft hydrogels compared to stiff hydrogels (fig. S7D). Similarly, 55.7% of differentially accessible ATAC-seq peaks that overlapped a chromatin loop in cells cultured on stiff hydrogels were more accessible on stiff hydrogels compared to soft hydrogels (fig. S7D). These results indicate that long-range chromatin interactions, in part, may facilitate the observed changes in gene expression between cells cultured on soft or stiff hydrogels.

Mechanoenhancers increase gene expression on stiff materials

We next determined if any stiffness-sensitive chromatin regions could harbor functional putative regulatory elements (pREs). We first noted that one of the most differentially accessible regions across 1 and 50kPa hydrogels was an intergenic pRE located ~14kb upstream of *FZD2* (fig. S13 and supplementary text 2). This region had exogenous enhancer activity in reporter constructs that responded to small molecule perturbations in cell contractility. dCas9-KRAB repression of this upstream distal pRE was found to regulate FZD2 activity, confirming the role of this region as a mechanically-responsive enhancer (or "mechanoenhancer") of FZD2 that becomes activated on stiffer materials.

First release: 25 September 2025

Given that cell contractility is necessary to maintain the stiffness-dependent changes in chromatin accessibility observed on stiff hydrogels (fig. S5), we next investigated cisregulatory mechanisms controlling the non-muscle myosin genes MYH9, MYH10, and MYH14. These genes encode nonmuscle myosins IIA IIB, and IIC respectively, which are the primary drivers of cellular contractility in non-muscle cells (48). In HFF cells, MYH9 was the predominantly expressed non-muscle myosin and the only one to exhibit ECM stiffnessdependent changes in expression, with a large absolute transcriptional shift between 1 and 50kPa hydrogels (Fig. 2A). Our ATAC-seq analysis identified 14 stiffness-sensitive chromatin regions within 100kb of the MYH9 transcriptional start site (TSS), so we next tested if any of these cis-regulatory regions might be regulatory elements that modulate MYH9 expression in response to mechanical cues.

To perturb the epigenetic state at any specific genomic locus, we utilized CRISPR interference (CRISPRi) with the dCas9KRAB epigenome editor. dCas9KRAB induces epigenetic silencing by recruiting factors that catalyze the addition of repressive histone marks at the target site (e.g., H3K9me3), also leading to the removal of active histone marks (e.g., H3K4me3/H3K27ac) and decreased chromatin accessibility (49, 50). We first performed a CRISPRi screen with a gRNA library tiling all ATAC-seq peaks in HFF cells within ±440 kb of the MYH9 TSS regardless of whether they were mechanically sensitive (114 regions, 5,192 gRNAs) (Fig. 2B). Cells were fixed, stained for MYH9 (NMIIA), sorted into MYH9-high and MYH9-low expression bins, and compared for their distributions of gRNAs (supplementary text 3, fig. S8, tables S9 and S10, and methods). We identified five pREs as strong regulators of MYH9 protein expression, including two in the MYH9 promoter/TSS region and three within a ~5 kb section of intron 3 of MYH9 (Fig. 2, C and D). Of the three pREs in intron 3, only the first pRE was differentially accessible between soft and stiff hydrogels (Fig. 2E). Further analysis of H3K27ac across diverse ENCODE biosamples around the sub-region of differential accessibility showed low H3K27ac signal in suspension (e.g., K562 cells) or weakly adherent cell lines, but greater H3K27ac signal across increasingly adherent and contractile cell lines (e.g., HUVEC/HSMM; Fig. 2F). Singleton validation of the screen hits confirmed the cis-regulatory role of all of three hit pRE regions (fig. S9), with targeting of the stiffness-sensitive intron 3 pRE#1 reducing MYH9 mRNA levels by as much as 54% compared to controls (Fig. 2G), to expression levels consistent with those seen on soft ECM (Fig. 2A). Targeting the MYH9 promoter resulted in ~87% repression of MYH9 transcript levels (Fig. 2G). Immunostaining with flow cytometry analysis confirmed similar trends in MYH9 protein levels 15 days after transduction of the gRNA along with dCas9^{KRAB} (fig. S10). Vinculin-containing focal adhesions (FAs) are key mechanoresponsive subcellular

structures, and their size and shape are strongly dependent on myosin activity (48, 51). Repression of the MYH9 promoter on tissue culture plastic showed substantial changes in cell size and a near complete loss of vinculin-containing focal adhesions (fig. S11). However, repression of the pRE#1 mechanoenhancer on rigid tissue culture plastic resulted in significantly reduced FA size and altered actin organization (Fig. 2, H to K, and fig. S11), indicating a lower contractile state of these cells compared to cells that received the nontargeting control gRNA. Thus, the MYH9 intron 3 pRE#1 functions as a mechanoenhancer and dictates MYH9 expression in response to ECM stiffness cues.

Nuclease-active Cas9 and densely tiled saturating gRNA libraries can be used to determine key motifs involved in enhancer function by introducing a variety of disruptive small insertions and deletions through non-homologous end joining (NHEJ)-based DNA repair (52). Sequence changes in cells with a loss of enhancer function are then used to identify key transcription factor motifs. We adapted this Cas9 screening approach to identify motifs in the MYH9 intron 3 mechanoenhancer that control MYH9 expression. Using a stable HFF-Cas9 cell line, we introduced all 64 potential gRNAs tiling across the MYH9 intron 3 mechanoenhancer, and sorted cells based on MYH9 protein expression as the screen endpoint (Fig. 2L and table S11). We identified three gRNAs that substantially decreased MYH9 expression on TCP relative to the other gRNAs across the mechanoenhancer (Fig. 2M). Of these gRNAs, gRNA #24 targeted regions overlapping an SRF/CaRG motif and gRNAs #43 and #65 both overlapped an HLTF (helicase like transcription factor) motif (Fig. 2, N and O). Upon delivery of these individual gRNAs, MYH9 mRNA expression was significantly decreased, with a maximum of ~30% repression by gRNA #24 (Fig. 2P). Cytosolic G-actin ratios regulate the mechanically responsive nuclear shuttling of MRTF-A, which then interacts with DNA-bound SRF to further regulate transcription (17). In further support of this SRF motif region being critical for MYH9 mechanoenhancer activity, the transcription factor footprinting analysis showed signals suggestive of enriched protein binding around this site that was increased on 50 kPa hydrogels (fig. S12). HLTF is a key member of the SWI/SNF complex, which has been implicated in actin-based YAP/TAZ release and subsequent DNA binding (53). Together, these results support that actinassociated mechano-signaling processes drive MYH9 mechanoenhancer activity.

An intronic mechanoenhancer of BMF is more active on soft materials and is a key driver of the ECM stiffness-driven apoptotic response

Low substrate stiffness, reduced adhesion, and limited cell spreading have been shown to increase apoptosis or adipogenesis (7, 8, 54, 55). Apoptosis triggered by loss of ECM

engagement is termed anoikis (56, 57), and developing resistance to anoikis is a key step in cancer progression (58). From our RNA-seq analysis, we noted that BMF, a key transcriptional effector of anoikis, was strongly up-regulated on soft substrates (Fig. 3A). We also identified a cluster of ATACseq peaks near BMF that were significantly more accessible on soft hydrogels (Fig. 3B). To examine if these peaks function as regulatory elements of BMF transcription, we cloned the genomic DNA from the top three differentially accessible regions (pRE1-3) into a luciferase reporter plasmid and transfected these reporter plasmids into HFF cells cultured on TCP. Luciferase activity was measured after 24 hours. Since BMF transcription was increased in the low contractility context of soft materials, we hypothesized that the addition of ROCKi Y-27632 would further increase luciferase activity. Only BMF pRE#1 in intron 4 demonstrated any basal enhancer reporter activity on TCP, which was significantly increased following treatment with 10 µM Y-27632 compared to DMSO, while other regions remained at basal levels (Fig. 3C). This indicates that pRE#1 enhancer activity is increased in low-contractility environments, further supporting the function of this region in driving increased BMF expression preferentially on soft substrates.

We next tested the ability of *BMF* pRE#1 to regulate *BMF* transcription and anoikis. Latrunculin-A (LatA) treatment is a canonical model system for anoikis that is used to depolymerize the actin cytoskeleton to induce loss of FAs and integrin engagement to mimic loss of adhesion to the ECM (59). We transduced HFF cells with dCas9KRAB and either a nontargeting gRNA or a gRNA targeting BMF pRE#1 or the BMF promoter. After eight days, we evaluated BMF mRNA levels. Treatment with LatA increased BMF expression ~60-fold compared to DMSO-treated cells (Fig. 3D). Epigenetic repression of BMF pRE #1 and the BMF promoter reduced this LatAdependent increase in BMF expression by ~60% and ~85%, respectively (Fig. 3D). We then assessed changes in apoptosis by measuring caspase-3/7 activity using a luciferase reporter system 14 days post-transduction (8 days +LatA). Repression of BMF pRE #1 reduced LatA-induced apoptosis by ~50%, while repression of the promoter completely prevented LatAinduced apoptosis relative to the DMSO-treated control condition (Fig. 3E). These observations were further supported by direct measures of cell number, wherein cells were seeded onto tissue culture plastic and one day later challenged with LatA for three days prior to fixation and cell counting. BMF promoter epigenetic repression was found to completely block LatA-induced changes in cell number, and BMF enhancer repression showed significantly reduced cell number compared to cells treated with a non-targeting gRNA (Fig. 3F), suggesting increased cell death or reduced proliferation. Collectively, these data show that BMF pRE#1 acts as a mechanoenhancer of BMF, becomes activated on softer ECM

stiffness, and regulates the apoptotic cellular response in states of reduced cytoskeletal engagement and ECM attachment.

High-throughput CRISPR screening identifies key mechanoenhancers regulating cellular growth and migration

To identify cis-regulatory elements that contribute most strongly toward mechanosensitive cellular behaviors, we performed high-throughput CRISPRi screening with cellular growth and migration as the phenotypic readouts. We generated a library of 21,458 gRNAs targeting the top 1000 nonpromoter ATAC-seq peaks, ranked by their increased accessibility on stiff hydrogels (tables S4 and S8). We also included gRNAs targeting the promoters of 53 genes known to modulate migration (60) as positive controls, and 1000 non-targeting gRNAs as negative controls. HFF cells were transduced with the library and then assessed for changes in growth or migration (Fig. 4A). For the growth screen, gRNA enrichment was determined on day 8 and day 29/30 (after ~14 population doublings). The migration screen involved two consecutive overnight transwell assays at eight days post-transduction, with gRNA enrichment compared between migrated and non-migrated cells (methods).

We observed strong negative effects on cell proliferation when targeting the promoters of the positive control DepMap essential genes (e.g., GPKOW, EIF3E, ACTG1, CSNK1A1, PCYT1A, PTPN23) (61, 62) and genes related to proliferation (e.g., ABL1, ITGB8, G3BP2, OTUD6B) (63, 64). In the migration screen, we found that promoter-targeted repression of key genes known to influence cell adhesion and force generation, including ITGAV, ACTG1, CDC42, and TPM3 (60), led to decreased cell migration (fig. S14). Perturbation of mechanically sensitive pREs led to effects comparable to those observed in the positive control promoter targets (fig. S14). Zscore enrichment was found to be driven by a small fraction of the gRNAs across both screens (Fig. 4, B and C), consistent with previous reports on epigenetic editing of regulatory elements (30). In total, we identified 58 pREs regulating migration and 50 pREs affecting proliferation, with 7 regions regulating both phenotypes (Fig. 4D, tables S12 and S13, and methods). Although ECM stiffness is known to influence both cell proliferation and migration (65, 66), we found no correlation between the phenotypic scores across pREs regulating either or both phenotypes (fig. S15A). Furthermore, perturbations of pREs that regulated only migration or both phenotypes had greater effects on migration compared to pREs that regulated only growth (fig. S15B). There was no difference between the same groups for the growth phenotype. We next asked whether any of the pREs from the growth and migration screens were functional in other cell types and tissues by examining their overlap with accessible chromatin regions in

First release: 25 September 2025

95 ENCODE biosamples (table S14, supplementary text 4, and fig. S16). pRE hits from functional screening had the greatest overlap with accessible chromatin regions for highly adherent cell types (e.g., skeletal muscle myoblast and fibroblast lineages, 96-99% of pREs in accessible chromatin) and the least overlap with suspension cell types (e.g., T cells and K562 cells with only 19% of pREs accessible). Together, these analyses show the functional pREs that become activated on stiff ECM are shared across multiple cell types and can be active across many adherent cell types.

Single cell CRISPRi screening identifies gene targets regulated by mechanoenhancers that drive cellular growth and migration

To identify gene targets regulated by the pREs identified in the proliferation and migration screens, we performed CRIS-PRi followed by single cell RNA-seq. We designed a sublibrary of gRNAs targeting 87 pREs, selecting those with the largest effect sizes from the previous screens, with 10 gRNAs per pRE (methods). This library also included positive controls of promoter-targeting and known enhancer-targeting gRNAs, and 100 non-targeting negative control gRNAs, resulting in a total of 1,005 gRNAs (table S15). We transduced HFF cells expressing dCas9^{KRAB} cultured on TCP with this gRNA library at a multiplicity of infection (MOI) of 0.33, and eight days post-transduction we profiled 103,440 quality single cell transcriptomes (Fig. 4E). We recovered a median of 1 gRNA per cell and identified an average of 159 cells containing each gRNA (fig. S17, A and B). To link pREs to their gene targets, we compared the expression of all genes within ±1 Mb of each targeted pRE in cells that received the gRNA against those that did not receive the gRNA (Fig. 4F, table S16, and methods). This ±1Mb window was chosen as previous studies suggest that most cis-regulatory interactions occur within this genomic distance (29, 67-69).

In total, we identified 201 significant pRE-gene connections total and connected 65 pREs to at least one gene (74.7%, 65/87), with a median of 2 genes linked to every significant pRE and 1 pRE to each gene with at least one connection (fig. S17, C to E, and methods). In contrast to the expectation that a cis-regulatory element targets its nearest gene, we found that a median of 3 and a mean of 6.5 genes were "skipped" by pREs to regulate a more distant target gene (methods). In fact, 37.1% of pRE-gene links skipped at least one other gene, and 21.8% skipped five or more genes (fig. S22, A and B, and supplementary text 5). One notable pRE had over 10 gene linkages and was accessible in multiple ENCODE biosamples ("ubiquitous" cluster in fig. S16, fig. S18, and supplementary text 6). For the positive controls, we recovered 92% of expected promoter-targeting gRNA and 100% of enhancer-targeting gRNA connections with their target gene (fig. S19A), with all effects showing significant decreases in target gene

expression as expected (fig. S19, B to E). Notably, perturbation of the MYH9 intron 3 enhancer (Fig. 2) reduced MYH9 expression and also up-regulated two additional genes, APOL2 (~90kb downstream) and RAC2 (~900kb upstream) (table S16). Across the identified pRE-gene linkages, the magnitude of gene repression correlated positively with the basal expression level of the target gene, with more highly expressed genes showing stronger repression (fig. S20A). Gene expression changes diminished as the distance between the pRE and the target gene increased (fig. S20, B to D), consistent with previous work (29). To determine the taxonomy of the pREs, we intersected the pREs with predicted cis-regulatory elements in human cell types and tissues (70) and chromatin state annotations in HFF cells (71). The majority of pREs identified by both bulk and single cell screening approaches overlapped distal enhancer-like signature (dELS) elements and genomic regions annotated as having "Enhancer"-like chromatin state (fig. S21, A to D).

Genes linked to mechanically regulated pREs play key roles in diverse cellular functions

Next we examined the downstream target genes regulated by pREs that showed strong functional significance in driving growth or migration in our screens. Initially, we examined the effects of perturbing the positive control MYH9 promoter and its associated mechanoenhancer. We observed that targeting the MYH9 intron 3 mechanoenhancer led to ~50% of the repression as targeting the MYH9 promoter (Fig. 4G), in agreement with the previous singleton gRNA experiments (Fig. 2G). We compared the effect size of the top eight pREgene linkages from the growth and migration screens (ranked by phenotype Z-score) to the impact on target gene expression in the single cell RNA-seq screen (Fig. 4, F and G). For comparison, we also included the top two pRE-gene linkages that most strongly influenced gene expression without any requirements for functional screen enrichment (Fig. 4F). Of note, pRE#62 showed the strongest combination of effects on gene expression and migration, and was found to modulate the transcription of CYR61. Similarly, perturbation of pRE #740 led to strong effects on both CTGF expression and cellular growth (Fig. 4, F and G). Both CYR61 and CTGF are canonical YAP/TAZ target genes, with CYR61 being strongly linked to migratory phenotypes across many cell-types (72), and CTGF playing key roles in cellular growth (73, 74). Using this single cell CRISPRi screening approach we further identified pREs as strong drivers of cell migration that also changed the expression of genes known to function in mechanoresponsive and cell migration-related pathways (Fig. 4F). These genes include CYR61 (CCN1, fig. S23), DUSP4 (fig. S24, A and B), FAM98B and RASGRP1 (fig. S25), and RANGAP1 (fig. S26) (supplementary text 7). Similarly, perturbation of pREs driving cellular growth led to changes in expression of genes with

First release: 25 September 2025

known functions in cell proliferation, including *CTGF* (also known as *CCN2*, Fig. 5E), *NF2* (fig. S23, C and D), and *SKP2* (fig. S27), as well as in genes not previously linked to cell proliferation including *RFLNB* (fig. S24, C and D) (supplementary text 8).

To validate the pRE-gene linkages identified in the single cell RNA-seq CRISPRi screen, we selected 13 pRE-gene connections for singleton gRNA validations and validated 30 gRNAs across these connections in HFF cells. We delivered individual gRNAs to the same HFF CRISPRi cell line cultured on TCP and assayed for changes in gene expression via RTqPCR at eight days post-transduction. We confirmed 10 out of 13 pRE-gene connections, validating mechanoenhancers of CTGF, RFLNB, SKP2, NF2 (growth) and CYR61, DUSP4, FAM98B, RASGRP1, RANGAP1, and ZC3H7B (migration) (Fig. 4, F and G; figs. S23 to S27; and table S17). The changes in mRNA expression in the validations correlated with the gene expression changes observed in the single cell screen (fig. S28). Collectively, these data demonstrate that many of the identified pREs are bona fide mechanoenhancers that regulate the expression of key genes and ultimately alter cell growth and migration in response to ECM stiffness cues.

Epigenetic repression of validated mechanoenhancers impairs cellular mechanosensitivity across cell types and ECM stiffness

Next, we selected three validated mechanoenhancers for additional analysis (SKP2, CTGF, and MYH9) based on their responsiveness to both material stiffness and cell contractility inhibition, as well as their implicated role in fibrosis (13, 75-77). Specifically, we first tested the effect of epigenetic repression of these mechanoenhancers on transcription in HFFs and A549 cells cultured on the fibronectin-coated hydrogel system (1 and 50 kPa) as well as TCP on which the screens were performed. All three mechanoenhancers were accessible and responsive to CRISPRi under at least one condition in each cell type (Fig. 5). The SKP2 mechanoenhancer (~4kb downstream of the TSS, Fig. 5A) was responsive to CRISPRi on TCP, but not on the hydrogels in HFF cells (Fig. 5B). However, in A549 cells, this SKP2 mechanoenhancer was repressed by CRISPRi in all conditions and showed increased magnitude of response with increasing stiffness (Fig. 5C). The intergenic CTGF mechanoenhancer (~133kb upstream of the TSS, Fig. 5D) showed strongly increasing transcriptional contributions with increasing ECM stiffness in HFF cells (Fig. 5E). In contrast, the CTGF mechanoenhancer showed more modest activity and limited stiffness response in A549 cells (Fig. 5F). Finally, transcriptional contributions from the MYH9 intron 3 mechanoenhancer (~57kb downstream of the TSS, Fig. 5G) were strongly stiffness-dependent in both cell types (Fig. 5, H and I). Epigenetic repression of each mechanoenhancer nearly completely removed stiffness-driven

increases in transcription, resulting in levels of transcription that were similarly low across all material conditions.

Tissue fibrosis is associated with changes to ECM composition and stiffening of local matrix mechanical properties that can provide positive feedback to pathological progression (78). Gene targets of our identified mechanoenhancers have been implicated in fibrotic disease, including of CTGF, which is a hallmark of fibrosis across numerous tissues and CTGF expression is specifically found to be up-regulated in patients diagnosed with idiopathic pulmonary fibrosis (IPF) (75). To determine if these validated mechanoenhancers are functional in cell types relevant to fibrotic disease, we characterized activity of these mechanoenhancers in primary human lung fibroblasts isolated from four control healthy donors and four donors with IPF (Fig. 5, J to L). Lung fibroblasts were harvested from tissue using a magnetic-activated cell sorting (MACS)-based enrichment approach, cultured, transduced with a lentivirus encoding dCas9KRAB, and subsequently transduced with an additional lentivirus encoding a gRNA targeting either the SKP2, CTGF, or MYH9 mechanoenhancers. First, we studied IPF and healthy donor fibroblasts stimulated with PDGFa as a baseline mitogen allowing for cell outgrowth (79, 80). All primary fibroblasts were seeded on rigid TCP to induce strong baseline fibrogenic activation and assess mechanoenhancer activity. Immunostaining revealed modestly increased alpha smooth muscle actin (αSMA) , a marker of fibroblast activation, in the IPF-derived fibroblasts relative to cells from healthy donors under these conditions (Fig. 5K). At baseline, the expression of CTGF, SKP2, and MYH9 was generally similar across healthy and IPF donor fibroblasts with PDGF α treatment alone (Fig. 5L). This is potentially due to the rigid TCP culture conditions outweighing the effect of the disease state of the original donor in driving activity of these mechanoenhancers. We also compared the transcriptional responses between healthy lung fibroblasts activated in vitro with TGF\$1 to induce the fibroblast to myofibroblast transition implicated in fibrosis (81). Strongly increased immunostaining of α SMA confirmed that TGF\$1 treatment successfully activated healthy lung fibroblasts relative to the baseline PDGF α + TCP treatment (Fig. 5K). In cells treated with a non-targeting gRNA, TGFβ1 treatment reduced SKP2 expression by ~60%, increased CTGF by nearly 100-fold, and slightly increased MYH9 expression compared to the baseline PDGFα treatment (Fig. 5L).

We next used CRISPRi of the SKP2, CTGF, and MYH9 mechanoenhancers to assess their specific transcriptional contributions across these eight donor-derived cell lines and two fibrotic model culture systems. Notably, repression of these mechanoenhancers reduced transcriptional activity of their target genes across all eight donor lines (Fig. 5L). This strong conservation across samples suggests a broad role of these mechanoenhancers in gene regulation. Moreover, epigenetic repression of the CTGF mechanoenhancer prevented 96% of the 100-fold increase in transcription induced by treatment of healthy donor fibroblasts cultured on TCP supplement with TGF_{\beta1}. These findings highlight the critical, context-dependent role of these mechanoenhancers in regulating gene expression in response to mechano-chemical stimuli, including ECM stiffness and pro-contractile soluble cues. Epigenetic editing of these mechanoenhancers effectively reduced ECM stiffness-mediated transcriptional responses and prevented the activation of genes known to be associated with the fibroblast-to-myofibroblast transition in isolated lung fibroblasts from healthy and IPF donors, including CTGF and MYH9 (75, 82).

Conclusions

Using complementary modern technologies for functional genomics, we identified a class of cis-regulatory elements that are responsive to changes in material stiffness, which we refer to as "mechanoenhancers." Mechanoenhancers could be more active on either soft or stiff substrates and were dependent on intracellular contractility. Functional screening revealed that some pREs could act as key transcriptional drivers of fundamental cell processes, including ECM mechanosensing, apoptosis, cellular growth, and migration. Notably, these mechanoenhancers were active in lung fibroblasts isolated from healthy and IPF donors when cultured on tissue culture plastic (Fig. 5). The gene-to-mechanoenhancer connections identified through unbiased transcriptome-wide screening revealed that, unlike promoter-based regulation, mechanoenhancers often regulate multiple downstream gene targets, with a median of two linkages per pRE, spanning large genomic distances (figs. S17 and S20). This provides one example of how mechanical and chemical cues, particularly those that regulate contractility, may combine to regulate mechanoenhancers. Together, this work suggests that epigenome editing of mechanoenhancers can be an effective means of decoupling mechanically-driven behaviors from the mechanical stimuli.

On stiff ECM conditions, we found that the activities of multiple mechanosensitive signaling pathways likely drive the activity of mechanoenhancers. We observed that mechanoenhancers were enriched with binding sites for canonical mechanosensitive transcription factors including TEAD and SRF/CarG (Figs. 1 and 2 and figs. S3 and S4) (26, 40, 45), in addition to motifs for protein families that have not previously been strongly associated with mechanosensing pathways (e.g., LEF, FOXA, HNF) (figs. S3 and S4). A key question for future work will be determining how multiple mechanosensitive proteins and pathways work in combination to regulate changes in gene expression at mechanoenhancers.

While mechanosensitive signaling pathways that increase

transcription on stiff ECM are well-described, comparatively less is known about those that drive increased transcription preferably on soft ECM. Previous studies examining chromatin accessibility in soft hydrogel conditions with ATAC-seq did not find peaks with increased accessibility preferentially on soft materials (45, 47). However, through the use of onplate ATAC-seq processing that did not require de-adhesion of cells prior to collection, we identified a large subset of peaks that were more accessible on soft ECM (Fig. 1, E to G), with one region preferentially open on soft ECM found to function as a BMF mechanoenhancer. One potential mechanism driving this pattern of activity is stiffness-induced epigenetic repression. For instance, dynamic mechanical stretch can induce the H3K27me3 repressive histone mark and transcriptional down-regulation (20-22). YAP-based epigenetic repression around this BMF mechanoenhancer on TCP was previously noted in non-small cell lung cancer (NSCLC) treated with kinase inhibitors, further supporting a stiffnessinduced epigenetic repression mechanism (83) (supplementary text 9). A key aspect of future work will be to determine if stiffness-induced epigenetic repression is a common mechanism of mechanoenhancer regulation.

One common characteristic of mechanically-induced disease states, including cancer and fibrosis, is the excessive activation of positive feedback loops that amplify mechanical signaling and drive disease progression (78, 84-87). In this process, initial increases in ECM stiffness trigger gene expression changes that further sensitize cells to, or increase, ECM stiffness cues. This work identified mechanoenhancers that drive the activation of multiple genes likely contributing to these positive feedback loops, including CTGF, CYR61, MYH9, RFLNB, RANGAPI, RASGRPI, and NF2. For example, we found that the MYH9 mechanoenhancer drives increased expression of MYH9 in response to ECM stiffness, thereby initiating a possible mechanical signaling loop wherein enhanced contractility potentially further activates the mechanoenhancer which sensitizes the cell ECM stiffness changes (87). Another potential example of propagating mechanical feedback loops is through the mechanoenhancer RANGAPI, a key factor in cytoplasmic-nuclear shuttling that promotes increased import into the nucleus (15, 88). In this proposed positive feedback loop, mechanical forces activate the mechanoenhancer resulting in increased RANGAP1 expression, which potentially promotes nuclear import and further increases the sensitivity of that cell to subsequent mechanical signals. This extends current models of how mechanical force can directly bias nuclear transport (89), by suggesting that this process may be further tuned by transcriptional feedback from mechanoenhancers of key nuclear transport machinery like RANGAPI.

By epigenetic editing of mechanoenhancers activated by increased ECM stiffness, we could prevent increased expression of key genes (e.g., CTGF) associated with fibrotic disease. These effects are likely due to reduced activation of mechanosensitive positive feedback loops. Moving forward, epigenome editing of mechanoenhancers will be a powerful tool for precisely engineering cellular responses to the mechanical microenvironment, and could have widespread applications in both cell engineering and gene therapy. Therapeutic modulation of known gene targets implicated in mechanically-driven disease states like cancer, atherosclerosis, fibrosis, and aging has historically proven to be challenging, as strong modulation of genes and their products can disrupt both pathogenic and essential functions. If therapeutic epigenome editing of key mechanoenhancers can modulate pathogenic positive feedback loops while leaving essential signaling functions intact, this approach may enable novel treatment strategies in mechanosensitive diseases.

Materials and methods Cell culture for RNA/ATAC-seq

Primary human neonatal fibroblasts (HFF cells) were acquired from ATCC (CRL-2097) and cultured in DMEM with 10% FBS, 1% AntiAnti, and 1% NEAA (Sigma) on TCP. A549 cells were cultured in F-12K Medium from ATCC (30-2004) with 10% FBS. All work was performed within 30 doublings from the initial passage of the vial.

RNA-seq and Omni-ATAC-seq

Cell culture and soft hydrogel processing

Polyacrylamide hydrogel 35 and 150 mm PetriSoft EasyCoat dishes (Matrigen) with an Elastic Modulus of 1 kPa ("soft") and 50 kPa ("stiff") were used for all NGS experiments. These dishes were incubated for 5 min with sterile PBS, rinsed two more times with sterile PBS, followed by addition of 10 ug/mL fibronectin (Sigma) for 30 min at room temperature. Fibronectin was then removed, and dishes were rinsed twice with sterile PBS, followed by a 20-min incubation with complete growth media while cells were passaged. Media was removed from the dishes and cell suspensions were added and allowed to attach overnight.

Bulk RNA-seq

40k HFF cells were seeded on 35mm 50 kPa dishes and TCP dishes, while 70k HFF cells were seeded on 1 kPa 35mm dishes to achieve the same effective plating density due to slightly reduced HFF attachment rates (and spreading) on 1kPa hydrogels. Similarly, A549 cells were seeded on Matrigen T75 flasks (1 kPa and 50 kPa) at slightly variable densities to account for reduced cell attachment on softer substrates (2 million cells and 1.25 million cells, for 1 and 50 kPa flasks). 20 hours after seeding, cells were trypsinized spun down at 300g for 5 min and then RNA was isolated from the cells using the Norgen Total RNA Purification Kit

(#17250) according to the manufacturer's protocol, and samples were run on an RNA TapeStation (Agilent) to verify all samples had a RIN score > 8. cDNA Libraries were built from our RNA inputs using the TruSeq Stranded Library Prep Kit (Illumina #RS-122-2101) according to manufacturer's instructions. Quality control was performed by running the amplified libraries out on a High Sensitivity D1000 Tapestation (Agilent) to confirm expected size, and Qubit dsDNA HS assays were performed to determine a final concentration. Libraries were diluted to 10nM and pooled together in equal volumes, followed by sequencing performed on an Illumina HiSeq 2500 using a 50bp PE RapidRun kit. Resulting reads were subjected to adapter trimming using Trimmomatic v0.32 (90), aligned to GRCh38 with the STAR v2.4 aligner (91), and counts were retrieved using featureCounts (92) from subread version 1.4.6p4 with Gencode v22 gene annotations used as reference. Differential expression analysis was performed using edgeR quasi-likelihood methodology (93) and data was visualized using Degust (94) and Rstudio. Genes with significant differential expression were determined using a threshold of FDR < 0.05 and absolute value of Log₂(FC) > 0.5.

Omni ATAC-seq

HFFs were seeded on 35mm Matrigen dishes of varying stiffness (1, 12, 50 kPa elastic modulus) at slightly variable densities to account for reduced cell attachment on softer substrates (70k, 45k, 40k HFF cells seeded per group) and allowed to culture for 20 hours. A549s were seeded in a similar fashion with Matrigen T75 flasks (1, 50 kPa elastic modulus) seeded with either 2 million and 1.25 million cells per flask, respectively and allowed to culture for 20 hours. For Y-27632 ROCKi experiments, the cells were seeded as normal, but 1 hour prior to harvest 10 µM Y-27632 ROCKi (StemCell Tech) in growth media was added to the cells. For verteporfin (Sigma-Aldrich) and CCG-222740 (MedChemExpress) studies, these inhibitors were added 18 hours prior to harvest and used at 0.7 µM and 20 µM, respectively. The Omni-ATAC-seq protocol was used to minimize mitochondrial reads from the preps (95), however no trypsinization was used and instead on-plate disruption/removal of nuclei (using the digitonin present in the lysis buffer) was used to better preserve nuclear mechanical context and connectivity prior to transposition by the Tn5. Following the final PCR, libraries were cleaned with a 0.5x/1.8x double-sided SPRI clean. Libraries were subjected to quality control by determining the number of cycles required to reach 25% of the peak threshold in the diagnostic PCR, as well as running the amplified libraries out on a High Sensitivity D1000 Tapestation (Agilent) to confirm expected size, and Qubit dsDNA HS assays were performed to determine a final concentration. Libraries were individually diluted to 6nM and then pooled at equal volumes prior

First release: 25 September 2025

to sequencing on an Illumina HiSeq 4000 using a single lane of 50bp single end reads. FastQC (96) was used to identify read quality, and adapter reads were trimmed using Trimmomatic v0.32 (90) followed by Bowtie (97) alignment (v1.0) of the reads to the reference genome using the settings: -v 2 -best -strata -m 1 with duplicate reads removed using Picard MarkDuplicates (v1.13) and ENCODE hg38 blacklist reads removed using bedtools2 v2.25 (98). Peak calling was performed using MACS2 with narrowPeak settings and a threshold of FDR < 0.001 (99), and a master peak set was generated as the union set of all called peaks across every sample analyzed (224,906 unique regions total). Count matrices were made using featureCounts (92) and DEseq2 v1.36 was used for differential accessibility analysis (100). Annotation of genomic regions was performed using ChIPSeeker (101), interactive visualization of processed data was done using Degust (94) and Rstudio along with ggplot2 and tidyverse plugins were used to generate data visualizations. Sequencing-depth normalized ATAC bigWig files were generated using deeptools bamCoverage v3.0.1 (102). All motif analysis was performed using the HOMER suite (103).

Footprinting

A TOBIAS-based footprinting analysis was performed to assess differential transcription factor (DTF) binding in A549 cells and HFF cells under distinct conditions (1kPa vs 50 kPa). Replicates for each condition were merged using samtools (v1.21). The resulting BAM files were then sorted and indexed. To correct for Tn5 insertion bias, ATAC-seq BAM files and peak sets were processed by TOBIAS (version 0.17.1) ATACorrect with the hg38 reference genome (44), which generated corrected BigWig files for downstream analysis and visualization. TOBIAS FootprintScores were then applied to the corrected files and corresponding union peaks to generate footprint scores for each condition. DTF binding analysis was performed using TOBIAS BINDetect, with motif definitions from the JASPAR 2024 CORE vertebrates non-redundant database in MEME format. TOBIAS PlotTracks was used to visualize DTF footprints at specific genomic loci. ATAC-seq signal tracks and corresponding footprint scores from both 1 kPa and 50 kPa conditions were plotted across selected genomic regions defined in a custom BED file. High-confidence binding sites were overlaid as both sites and highlight tracks to emphasize regions of interest. Gene annotations were incorporated from the GENCODE v47 GTF file, and distinct color codes were applied to facilitate condition-specific comparison.

HiCAR

HFF cells were seeded on Matrigen T75 flasks (1 kPa and 50 kPa) at slightly variable densities to account for reduced cell attachment on softer substrates (2 million and 1.25 million).

After 20 hours, HiCAR libraries were prepared as previously described, with the following modification: glycine was added to a final concentration of 0.125 M and incubated at room temperature for 5 min to quench formaldehyde (104). This protocol included a rapid fixation step prior to Tn5 transposition. 200,000 crosslinked cells were used for each replicate. Nuclei were isolated using NPB buffer (5% BSA in PBS, 1mM DTT, 0.2% IGEPAL, Protease Inhibitor) and incubated with assembled Tn5 transposase in 1X TB buffer (33 mM Tris-AC pH 7.8, 66 mM KCl-AC, 10 mM Mg-AC, 16% DMF) at 37C on a rotator for 1 hour. Chromatin digestion was performed with MseI, followed by in situ ligation with T4 DNA ligase and DNA purification. Purified genomic DNA was further digested with NlaIII and circularized with T4 DNA ligase, followed by DNA purification and PCR amplification. After size selection, the libraries were sequenced using the Illumina Novaseq X.

The analysis pipeline to process the HiCAR libraries can

be found at https://nf-co.re/hicar/1.0.0 with the following parameters: --genome GrCh38, --profile singularity, --ensyme 'MseI', --restriction_sites '^TAA', --resample_pairs, qval thresh 0.01. Briefly, quality reads were determined us-FASTQC [https://www.bioinformatics.babraham.ac.uk/projects/fastq c/] then adapters were trimmed using cutadapt (105). Reads were aligned to the reference genome using bwa mem [https://bio-bwa.sourceforge.net/bwa.shtml#12]. Aligned reads were then processed using pairtools (106) and quality performed control was using pairsqc [https://github.com/4dn-dcic/pairsqc]. MACS2 (99) was used to call peaks and MAPS (107) was used to find genomic interaction loops. Differential analysis was performed using edgeR (93) and files for visualization were generated using Cooler (108) and Juicer (109). To compare the chromatin loops between ECM stiffness conditions, we used bedtools pairtopair with the -type parameter set to both, either, or neither (110). To compare the chromatin loops with the differentially accessible ATAC-seq peaks, we used bedtools pairtobed (110).

MYH9 locus screening

Library design and cloning

First release: 25 September 2025

Using the ATAC-seq data, every open chromatin region that was within 440 kb of the MYH9 TSS was used as input to generate an oligo pool. For each ATAC-seq peak, we included any gRNA that had a GuideScan specificity score of > 0.2, which has previously been shown to increase the quality of non-coding screens (111). This resulted in 114 peaks represented in the library, with an average of ~41 gRNA/peak. We also included 500 non-targeting gRNA as negative controls (112). This combined gRNA library of 5,192 gRNA was synthesized as an oligo pool by Twist Biosciences with common overhangs for cloning into our lentiviral backbone.

This oligo pool was PCR amplified, and a hU6-driven lentiviral gRNA vector (pBDC119) was then digested with Esp3I, gel purified, and then ligated along with the amplified oligo pool by Gibson assembly. Following a 1x SPRI cleaning, the Gibson assembly was transformed into Endura competent cells (Lucigen) according to the manufacturer's protocol, and cultured overnight before maxi-prepping the gRNA-library plasmid. A PCR amplicon across the gRNA region of the resulting plasmid was sequenced to a depth of ~100k-1M read pairs on an Illumina miSeq in order to verify coverage across the entire gRNA library (fig. S29).

Lentiviral generation and functional titering of MYH9 locus library

gRNA library plasmid was co-transfected into ~18M HEK293T cells along with two lentiviral packaging plasmids using Lipofectamine 3000 (ThermoFisher). 20 hours posttransfection, the transfection media was removed and fresh growth media was added. Media containing viral particles was removed one day later at 48 hours post-transfection and stored, replaced with fresh media and collected one day later before being stored at 4C. Combined media containing viral particles was filtered through 0.45 µm low-protein binding filters, and then concentrated using Lenti-X Concentrator (Takara Bio) according to the manufacturer's protocol. Functional titering to determine MOI was performed by transducing HFF cells across a 50x-10,000x dilution range of the viral stock, and then subjecting the cells to FACS-based cell sorting to identify what percent of the population was mCherry+ for each viral stock dilution.

CRISPRi locus screen

A stable HFF line was created using a lentiviral dCas9-KRAB construct [pLV-hUbC-dCas9-KRAB-2A-Blast (pJB289)], followed by the gRNA library being transduced at an MOI of ~0.33 and Puro selection for four days at 1 ug/mL. Cells were maintained for an additional four days, prior to trypsinization and fixation at Day 10 post-transduction. Following trypsinization with 0.25% Trypsin-EDTA for 5 min at 37C, trypsin was neutralized with 1X volumes of complete growth media following by 300g for 5 min centrifugation and aspiration of the supernatant, one rinse with 1X volume PBS followed by another centrifugation and aspiration leaving 200uL of PBS above the pellet. The eBioScience ICC Fixation kit (ThermoFisher) was used to fix/permeabilize cells according to manufacturer's instructions, with both reagents being equilibrated to room temp prior to usage. Fixation was performed through the addition of 500uL eBioSciences Fix/Perm Buffer (ThermoFisher) to the 200uL PBS and pellet, and incubation at room temperature for 20 min. At the end of this incubation 1X Permeabilization Buffer was added to 8mL total volume, spun at 600g for 5 min, followed by an additional perm buffer

rinse. Following this step: HFF cells were counted, and ~2M cells were removed to be used for unsorted controls, and ~500k cells were set aside to be control samples for single channel compensation controls. Immunostaining of MYH9 was performed using a AlexaFluor-488 conjugated Rabbit monoclonal anti-NMMIIA antibody (clone EPR8965, Abcam, #ab204675) at a ratio of 0.5 uL antibody per 300k HFF cells per 100uL of Perm Buffer which was determined to be the ideal staining ratio using an antibody titration series. HFF cells were incubated for 30 min at room temperature in the dark on a nutating rocker, a 600g for 5 min spin, and two repeats of 3mL 1X Perm Buffer rinse/spin cycles. Following the last spin down, cells were resuspended in FACS Buffer [1X PBS supplemented w/ 1% BSA (Sigma) and 0.5mM EDTA (Sigma)] at density of ~9M cells/mL and sorted. A SH800 Cell Sorter (Sony Biotechnologies) was used to separate out the top/bottom-expressing MYH9 fractions following munostaining. Compensation panels were set up using single channel expressing cell populations including untreated cells, antibody-only cells, mCherry-only cells. The top 10% and lower 10% of the MYH9 population was sorted off and used for downstream gRNA-enrichment analysis and sequencing.

gDNA recovery and library preparation

Cells were counted following sorting to verify enrichment, followed by DNA recovery/extraction from fixed cells using the PicoPure DNA extraction kit (ThermoFisher) according to manufacturer's instructions. Recovery digests were performed for 20 hours at 65C using up to 1.5M HFF cells per reaction volume. All gDNA was split between sample-indexed 100uL Q5 PCR reactions (up to ~340ng max input per 100uL reaction) to amplify out the gRNA protospacer from HFF cells. These PCRs from gDNA were run as follows [98C for 30s / 25x: 98C for 10s, 60C for 30s, 72C for 15s / 72C for 2 min] with primers in table S19, followed by individual PCRs being pooled together and subjected to a double-sided 0.65X/1X SPRI clean-up. Quality control was performed by running the amplified libraries out on a High Sensitivity D1000 Tapestation (Agilent) to confirm expected size, and Qubit dsDNA HS assays were performed to determine a final concentration. All libraries were pooled to an effective concentration of 4 nM and combined in equal volumes prior to sequencing on an Illumina MiSeq, using a v2 50 cycle reagent kit with Read1 being 21 cycles (protospacer) and index read 1 being 6 reads (sample barcoding).

MYH9 locus library analysis

First release: 25 September 2025

Resulting FASTQ files were aligned to a custom reference sequence corresponding to the given gRNA library using bowtie2 and all downstream analyses were performed in R. All gRNA were verified to be represented in the baseline

untreated library dat Day 8 post-transduction, and counts+1 for each gRNA were taken (to normalize for samples that dropped out in one condition) and normalized by sequencing depth for each library before downstream analysis (in counts per million reads sequenced, "CPM"). Due to the highly apparent strand bias in the positive-strand when targeting the MYH9 gene body (supplementary text 1), we only included the non-interfering gRNA from the negative strand (2,863 gRNA). A ratio was taken of the CPM for each gRNA of the low MYH9 expression group to high MYH9 expression group to identify whether the gRNA perturbation led to increases in enrichment in either expression bin. Next, for each screen replicate the Z-score was calculated for each gRNA relative to the control non-targeting gRNA population using similar methodologies as previously described in (6). First, each sample's ratio was converted to a log2 fold-enrichment, and population statistics for the negative control non-targeting gRNAs (median, standard deviation, gRNA number) were calculated. For each individual gRNA, the median of the negative control fold-enrichment was subtracted from each individual gRNA's log2 fold-enrichment value, and this value was further divided by the standard deviation of the negative control non-targeting gRNA population to get an individual Z-score relative to the negative control population. Raw Zscore values from both replicates were pooled to calculate pRE-wide effects. Phenotype scores (t-score based) were calculated as:

Phenotype Score =
$$U(pRE) - U(CTL) / \sqrt{\frac{Svar}{Nexp} + \frac{Svar}{NCTL}}$$

 $Svar = Var(pRE) * (N(pRE) - 1) + Var(CTL) * (Nctl - 1)$

Individual gRNA validations

For gRNA validations of all 5 hit pRE across the MYH9 locus (including the two promoter/exon1 regions). Oligos containing protospacer sequences were synthesized by IDT and Scloned into play the protospacer sequences were synthesized by IDT and Scloned into play the protospacer sequences were synthesized by IDT and Science into play the protospacer sequences were synthesized by IDT and Science into play the protospacer sequences were synthesized by IDT and Science into play the protospacer sequences were synthesized by IDT and Science into play the protospacer sequences were synthesized by IDT and Science into play the protospacer sequences were synthesized by IDT and Science into play the protospacer sequences were synthesized by IDT and Science into play the play the play the protospacer sequences were synthesized by IDT and Science into play the cloned pLV hU6-sgRNA hUbC-GFP-P2A-PuroR (Addgene plasmid #162335). Sanger sequencing was used to confirm the identity of the gRNA. Lentivirus was generated as previously described (methods). dCas9-KRAB expressing HFF cells were seeded onto TCP and transduced on day 0. 24 hours post-transduction, lentivirus was removed and replaced with fresh growth media. Puromycin selection was applied as described for the bulk screen, and cells were harvested nine days post-transduction. mRNA was isolated using the Norgen Total RNA Purification Kit (#17250) according to the manufacturer's protocol. 100 ng mRNA was used as input for cDNA amplification using the Invitrogen Super-Script VILO cDNA Synthesis Kit. For RT-qPCR, each reaction contained 1 uL cDNA, 7 uL H20, 1 uL Tagman probe for TBP, 1 uL Tagman probe for MYH9, and 10 uL Quantabio PerfeCTa FastMix II. Delta delta Ct analysis was performed in

Microsoft Excel. Graphpad Prism was utilized to conduct oneway ANOVA tests followed by Tukey's HSD for post-hoc testing. Significance is reported in Fig.s as follows: *p-value < 0.05, **p-value < 0.01, ***p-value < 0.001. Tagman probe information provided in table S20. A portion of the transduced cells for the MYH9-intron 3 pRE were propagated to day 15 and then subjected to MYH9 immunostaining and flow cytometry as described in the bulk screen section, with gain values held constant across all collections across samples. Populations were plotted to show shifts relative to transduction with the non-targeting gRNA. Noting high values of MYH9 promoter-targeting gRNA, we did a similar transduction and examined RNA expression at day 6 post-transduction and saw markedly lower levels of MYH9 expression, supporting the idea that MYH9 deficiencies in cytokinesis led to a dropout of transduced cells over longer timeframes (fig. S10).

Actin & vinculin labeling/immunostaining and focal adhesion imaging/analysis

HFF cells were seeded into 24 well-plates while being transduced with lentiviruses encoding an all-in-one construct that expressed dCas9-KRAB/hU6-gRNA (Addgene #71236) with the gRNA being either a non-targeting control, an gRNA for the MYH9 intron 3 enhancer, and a gRNA for the MYH9 promoter. Viral media was removed 20 hours later, and replaced with complete growth media. Puromycin selection was started 2 days post-transduction, wherein 1.5 ug/mL Puromycin was added to the growth media for 3 days prior to removal of the antibiotic selection and continued passaging of the cells for expansion. Six days post transduction our transduced HFF cells were seeded at at ~5k cells/well into μ-Slide 8 Well Glass Bottom (ibidi) chamberslides that were coated with 10 ug/mL fibronectin for 45 min at room temp and rinsed 1x with PBS prior to seeding. Following an overnight culture, the media was removed on the chamberslide and 200uL of 4% PFA was gently added to each well and cells were fixed at room temp for 15 min, rinsed 2x with PBS, and then permeabilized with a permeabilizing solution [PBS supplemented with 0.5% TritonX-100, 10% w/v sucrose, 600µM MgCl2] for 10 min at 4C. Permeabilizing solution was then removed from cells, followed by 2x PBs rinses, and blocked with a labeling solution [1% bovine serum albumin (Sigma) in PBS1 for 30 min at room temperature. Fresh labeling solution was added that contained a 1:300 dilution of a Rabbit monoclonal anti-Vinculin antibody (clone EPR8185, Abcam, #ab129002) and incubated in a nutating rocker in the dark overnight at 4C. The next morning the primary antibody was removed, rinsed 2x with labeling solution, and then a secondary solution that contained a 1:200 dilution of AlexaFluor488 Goat anti-Rabbit secondary (Thermo #A-11008), a 1:100 dilution of AlexaFluor647-Phalloidin (Thermo #A22287) and a

First release: 25 September 2025

1:5000 dilution of DAPI was added for 1 hour at room temperature on a nutating rocker in the dark. Following three PBS rinses, chamber-slide wells were mounted with Vectashield Antifade Mounting Media (Vector Laboratories, H-1000-10). All focal adhesion and actin imaging was performed using a 20x/0.8NA objective on a Zeiss AxioObserver 7 and a quad-bandpass filter. Focal adhesion morphometric characteristics were quantified using vinculin images input to an online web tool, the Focal Adhesion Analysis Server (FAAS) (113). For this analysis the minimum adhesion size was set to 0.21 µm² and the stdev thresh was set to 5.5. Each value is reported as the average across an individual cell within the group, with N=39-45 cells/per group for either the control non-targeting gRNA or the MYH9 intron 3 targeting gRNA.

MYH9 intron 3 saturation mutagenesis screening

Library design and cloning

For the MYH9 intron 3 pRE saturation mutagenesis library, we included any gRNA that was within the hit pRE from the MYH9 locus library, which resulted in 64 gRNA across the library. We also included 25 non-targeting gRNA (112) and 11 safe-targeting gRNA (114) as negative controls. This combined gRNA library of 100 gRNA was synthesized as an oligo pool by Twist Biosciences with common overhangs for cloning into our lentiviral backbone. This oligo pool was PCR ampLV hU6-sgRNA hUbC-GFP-P2A-PuroR plified, (Addgene plasmid #162335) was then digested with Esp3I, gel purified, and then ligated along with the amplified oligo pool by Gibson assembly. Following a 1x SPRI cleaning, the Gibson assembly was transformed into Endura competent cells (Lucigen) according to the manufacturer's protocol, and cultured overnight before maxi-prepping the gRNA-library plasmid. A PCR amplicon across the gRNA region of the resulting plasmid was sequenced to a depth of ~100k-1M read pairs on an Illumina miSeq in order to verify coverage across the entire gRNA library (fig. S29).

Lentiviral generation and functional titering

gRNA library plasmid pool was co-transfected into ~7.8M HEK293T cells along with two lentiviral packaging plasmids using Lipofectamine 3000 (ThermoFisher). 20 hours posttransfection, the transfection media was removed and fresh growth media was added. Media containing viral particles was removed one day later at 48 hours post-transfection and stored, replaced with fresh media and collected one day later before being stored at 4C. Combined media containing viral particles was filtered through 0.45 µm low-protein binding filters, and then concentrated using Lenti-X Concentrator (Takara Bio) according to the manufacturer's protocol. Functional titering to determine MOI was performed by transducing HFF cells across a 0.75x-100x dilution range of the viral stock, and then subjecting the cells to FACS-based cell sorting to identify what percent of the population was mCherry+ for each viral stock dilution.

MYH9 saturation mutagenesis screen

HFF cells were transduced with a lentiviral SpCas9 construct [FUGW-SpCas9-2A-HygroR (pVG54)], selected 100ug/mL hygromycin for 4 days with hygromycin in order to make a stable line. Following four passages the cells were frozen and used for subsequent screening experiments and validations. 600k HFF cells were transduced with lentivirus encoding the MYH9 intron 3 saturation pool. For screening, the same protocol was used as described above for the MYH9 CRISPRi locus screen, with 8 days of culture time prior to fixation, MYH9 immunostaining, FACS for the top/bottom 10% of cells, PicoPure gDNA recovery, and gRNA PCR and processing for enrichment across the low and high MYH9 expression bins.

Individual gRNA validations

For gRNA validations of all 3 hit gRNA that had significantly altered MYH9 expression and a non-targeting control gRNA, oligos containing protospacer sequences were synthesized by IDT and cloned into pLV_hU6-sgRNA_hUbC-GFP-P2A-PuroR (Addgene plasmid #162335). Sanger sequencing was used to confirm the identity of the gRNA. Lentivirus was generated as previously described above. Cas9 expressing HFF cells were seeded onto TCP and transduced on day 0. 24 hours post-transduction, lentivirus was removed and replaced with fresh growth media, cells were grown for 8 days (with 4 days of 1.5ug/mL puromycin selection). And for harvest cells were split with 500k cells for gDNA harvested following FACS (as detailed below) and RNA was harvested from 500k cells using a Norgen Total RNA Purification Kit (#17250). qPCR for MYH9 expression was performed as described above for the MYH9 locus screen.

gRNA validation indel enrichment across MYH9 expression bins

Additionally, 500k cells were processed similarly to the screen that included cell fixation, MYH9 immunostaining, FACS for the top/bottom 10% of cells, PicoPure gDNA recovery. A MYH9 intron 3 PCR was performed with an amplicon size of 666 bp. All gDNA was split between sample-indexed 100uL Q5 PCR reactions (up to ~340ng max input per 100uL reaction) to amplify out the gRNA protospacer from HFF cells. These PCRs from gDNA were run as follows [98C for 30s / 25x: 98C for 10s, 60C for 30s, 72C for 15s / 72C for 2 min] with primers in table S15, followed by individual PCRs being pooled together and subjected to a double-sided 0.65X/1X SPRI clean-up. Quality control was performed by running the amplified libraries out on a High Sensitivity D1000 Tapestation (Agilent) to confirm expected size, and Qubit dsDNA HS

First release: 25 September 2025

assays were performed to determine a final concentration. All libraries were pooled to an effective concentration of 4 nM and combined in equal volumes prior to sequencing on an Illumina MiSeq, using a v2 50 cycle reagent kit with Read1 being 21 cycles (protospacer) and index read 1 being 6 reads (sample barcoding). FASTQ reads were run through Crispresso2 (115) and indel enrichment in the low MYH9 bin was used to examine any overlapping TF motifs on common indel sites.

BMF/FZD2 enhancer characterization

Luciferase enhancer reporter assays

BMF/FZD2/MYH9 regions with differential accessibility were identified, and primers were designed to amplify these regions from gDNA isolated from HFF cell-lines. Briefly, 2x 25uL reactions were run wherein 30ng gDNA was input with 2x KAPA HiFi Hot Start MM and 0.75uL of 10uM PCR primers (table S21) for either Region #1/2/3 with an annealing temp of 63C. Sequences were confirmed via Sanger sequencing. These enhancer fragments were then assembled into an improved STARR-seq enhancer luciferase reporter vector (116) via Gibson assembly and clones were sequences via Sanger sequencing to confirm the fragment addition. To perform the luciferase assay, 15k HFF cells and 10k A549s were seeded per well into a 24 well-plate one day prior to transfection, and the day of transfection fresh media was added immediately prior to lipofection, with either DMSO only or blebbistatin (2, 10, 40 μM), Y-27632 (10 μM), nocodazole (10 μM) added. A Rho agonist, Rho Activator II #CN03 (Cytoskeleton Inc, #CN03) was also utilized at a final concentration of 1 µg/mL. Lipofectamine LTX (2.25uL per well for HFF, 2.5uL per well for A549) was used to transfect luciferase reporter plasmids (300ng for HFF, 500ng for A549) at a mass ratio of 90% experimental firefly luciferase plasmid to 10% Renilla luciferase pRL-CMV control plasmid (Promega) into cells. Cells were harvested 24 hours later and the Promega DualGlo Luciferase Assay was performed according to manufacturer's instructions, with luciferase activity read on a Promega GloMax Discover instrument (0.3s integration time). The average of four blank wells was then set as the background level and subtracted from all experimental values. Firefly luciferase values for each well were normalized to the Renilla luciferase values. Each experiment was further normalized to the performance of an empty luciferase reporter plasmid or FZD2 pRE reporter levels as baseline.

Latrunculin A induction experiment culture

Oligos containing protospacer sequences were synthesized by IDT and cloned into an all-in-one lentiviral vector expressing dCas9-KRAB-P2A-PuroR from an hUbC promoter and a gRNA from an hU6 promoter (Addgene plasmid #71236). All gRNA were selected as (-) strand gRNA to minimize the

strand-bias artifact (supplementary text 1). gRNA protospacselected for further use were BMF-pRE1-g3 ("CGTACATTCGTGACCGTCCC"), BMF-pRE1-g4 ("GGCCAGGCGCGGCCTGCAGT") and BMF-prom ("TCACGCCGAGGACTGACCAA"). Sanger sequencing was used to confirm the identity of the gRNA following cloning. Lentivirus was generated as described above for MYH9. HFF cells were transduced and seeded per well in a 24 well-plate on day 0, by adding 25uL of 20x concentrated virus along with 5k cells and growth media. 24 hours post-transduction, lentivirus was removed. Antibiotic selection was applied for four days and cells were grown for eight days post-transduction. At 9 days post-transduction cells were trypsinized, and were re-seeded at 5k HFF cells/well in a 24 well-plate for RNA experiments or 20k HFF cells/well in a 12WP for Cleaved Caspase 3/7 experiments. To model detachment, on 11 days post-transduction the media was replaced with growth media containing either DMSO or 0.5 uM Latrunculin A. Cells were harvested for RNA or CaspaseGlo 3/7 analysis one day following the addition of Latrunculin A.

Transcriptional expression and Cleaved Caspase 3/7-activity

mRNA was isolated using the Norgen Total RNA Purification Kit (#17250) according to the manufacturer's protocol. 100 ng mRNA was used as input for cDNA amplification using the Invitrogen SuperScript VILO cDNA Synthesis Kit. For RTqPCR, each reaction contained 1 uL cDNA, 7 uL H20, 1 uL Tagman probe for TBP, 1 uL Tagman probe for BMF or FZD2, and 10 uL Quantabio PerfeCTa FastMix II. Delta delta Ct analysis was performed in Microsoft Excel. Graphpad Prism was utilized to conduct one-way ANOVA tests followed by Tukey's HSD for post-hoc testing. Significance is reported in Figs as follows: *p-value < 0.05, **p-value < 0.01, ***p-value < 0.001. Tagman probe information provided in table S20. For Caspase-3/7 activity assays, HFF cells were subjected to the CaspaseGlo 3/7 Assay (Promega) and Cell TiterGlo Assay (Promega) according to manufacturer's instructions with luciferase values read out on a Promega GloMax Discover instrument (0.3s integration time). The average of two blank wells per assay was then set as the background level and subtracted from all experimental values. CaspaseGlo3/7 values per group were further normalized to cell counts per group determined from the CellTiterGlo data.

Bulk growth and migration functional CRISPRi screens

Library design and cloning

First release: 25 September 2025

The top 1000 regions from the ATAC-seq data that were increasingly-accessible on the stiff 50kPa substrates as compared to the soft 1 kPa substrate were used as input to generate an oligo pool (BDC03 ATAC libraries). For each

peak, we included any gRNA that had a GuideScan specificity score of > 0.2, which has previously been shown to increase the quality of non-coding screens (111). This resulted in 969 peaks represented in the library, with an average of ~20 gRNA/peak. We also included 1000 non-targeting gRNA (112), and 249 promoter-targeting gRNA for 83 positive control genes that have previously been shown to be key modulators of transwell migration following RNAi screens (60), with 3 gRNA per gene taken from the Dolcetto library (117). This combined gRNA library of 21,458 gRNA was synthesized as an oligo pool by Twist Biosciences with common overhangs for cloning into our lentiviral backbone. This oligo pool was PCR amplified, pLV_hU6-sgRNA_hUbC-GFP-P2A-PuroR (Addgene plasmid #162335) was digested with Esp3I and gel purified, and then the oligo pool and digested vector were ligated by Gibson assembly. Following a 1x SPRI cleaning, the Gibson assembly was transformed into Endura competent cells (Lucigen) according to the manufacturer's protocol, and cultured overnight before maxi-prepping the gRNA-library plasmid. A PCR amplicon across the gRNA region of the resulting plasmid was sequenced to a depth of ~100k-1M read pairs on an Illumina miSeq in order to verify coverage across the entire gRNA library (fig. S29).

Lentiviral generation and functional titering

Concentrated lentivirus was generated by the Duke Viral Vector Core from this plasmid pool. Functional titering to determine MOI was performed by transducing HFF cells across a 50x-10,000x dilution range of the viral stock, and then subjecting the cells to a qPCR-based titering protocol that has been previously described in detail (118).

Migration/growth pRE library screen

To perform screening, 600k HFF cells were transduced with the lentiviral library virus at 10.8 MOI to achieve a coverage of ~279 cells per gRNA. 20 hours after transduction the viral media was removed and replaced with fresh media, and starting 48 hours after transduction HFF cells were selected with 1 ug/mL puromycin for 4 days. Puromycin selection media was then removed and HFF cells were grown out for two additional days until day 8. On day 8, ~11M cells were counted and split between migration and growth screens. Coverage of at least 279 cells/gRNA was maintained for each group throughout the entire experiment.

Migration screening: On day 8, the bottoms of 8 um transwell inserts for 6WP were coated with 10 ug/mL fibronectin at room temp for 45 min and then rinsed 1x with PBS for 30 min before use. HFF cells were counted, placed into low serum conditions (0.2% FBS) and seeded at 240k cells per transwell insert across 18 inserts (~4.4M cells total). These inserts were placed into 10% serum and cells were allowed to migrate for 24 hours. Following this first day of migration,

each side of the membrane was separately trypsinized and counted, where 27% of the initial cells were recovered as migratory cells (~1.2M cells) and non-migrated cells were recovered from the top of the insert. These migratory and nonmigratory populations were re-seeded (separately by group) in the same way on new fibronectin-coated transwell inserts, with 4-5 inserts seeded at 240k cells/insert and allowed to migrate overnight. Following these two rounds of migration we trypsinized and collected the cells that either migrated twice or did not migrate twice (with a similar number of cells, 24%, being found to have migrated during this second round) and isolated gDNA using DNeasy kits (Qiagen).

Growth screening: HFF cells were counted on day 8 posttransduction, and gDNA from 2M HFF cells were harvested as the "Day 0" reference population using a DNeasy Blood and Tissue Kit (Qiagen). Around 1M HFF cells were reseeded into 15 cm dishes for ongoing culture, and then serially-passaged as normal for 14 doublings (either 21 days post-"Day0" for replicate 1 or 22 days post-"Day0" for replicate 2) while maintaining at least 1M cells per dish during each passaging. prior to the final gDNA harvest using a DNeasy Blood and Tissue Kit (Qiagen).

Library preparation and sequencing

All gDNA was split between sample-indexed 100uL Q5 PCR reactions (up to ~340ng max input per 100uL reaction) to amplify out the gRNA protospacer from HFF cells. These PCRs from gDNA were run as follows [98C for 30s / 25x: 98C for 10s, 60C for 30s, 72C for 15s / 72C for 2 min with primers in table S19, followed by individual PCRs being pooled together and subjected to a double-sided 0.65X/1X SPRI clean-up. Quality control was performed by running the amplified libraries out on a High Sensitivity D1000 Tapestation (Agilent) to confirm expected size, and Qubit dsDNA HS assays were performed to determine a final concentration. All libraries were pooled to an effective concentration of 4 nM and combined in equal volumes prior to sequencing on an Illumina MiSeq, using a v2 50 cycle reagent kit with Read1 being 21 cycles (protospacer) and index read 1 being 6 reads (sample barcoding).

Screen analysis

First release: 25 September 2025

Resulting FASTQ files were aligned to a custom reference sequence corresponding to the given gRNA library using bowtie2 and all downstream analyses were performed in R. All gRNA were verified to be represented in the baseline untreated library at day 8 post-transduction, and counts+1 for each gRNA were taken (to normalize for samples that dropped out in one condition) and normalized by sequencing depth for each library before downstream analysis (in counts per million reads sequenced, "CPM"). For migration screens: A ratio was taken of the CPM for each gRNA of the 2x migrated group to the 2x non-migrated group to identify migratory or non-migratory enrichment. For growth screens: A ratio was taken of the CPM of the Day 0 population relative to the final Day 21/22 population for each replicate. Next, for each screen replicate the Z-score was calculated for each gRNA relative to the control non-targeting gRNA population using similar methodologies as previously described (6). First, each sample's ratio was converted to a log2 fold-enrichment, and population statistics for the negative control nontargeting gRNAs (median, standard deviation, gRNA number) were calculated. For each individual gRNA, the median of the negative control fold-enrichment was subtracted from each individual gRNA's log2 fold-enrichment value, and this value was further divided by the standard deviation of the negative control non-targeting gRNA population to get an individual Z-score relative to the negative control population. Raw Z-score values from both replicates were pooled to calculate pRE-level effects. An individual gRNA was called as a "hit" if the Z-score was above 2 or below -2. pRE-level stats were generated by performing a Fisher's exact text relative to the non-targeting gRNA population, and a pRE-level was labeled significant for follow-up if the pval was less than 0.1. To select pREs for validation in single cell RNA-seq, we further selected the pRE hits that had more than one gRNA as a "hit" and had at least 10 gRNA/DHS in order to enable higher-powered analysis of the downstream data.

Comparison of phenotype scores between regions regulating growth, migration, or both phenotypes

Each significant region was labeled for the phenotype it regulated (one of growth, migration, or both). The phenotype (pZ) scores were compared between the three groups using a One-way ANOVA test followed by Tukey's post-hoc tests using the aov and TukeyHSD functions in R.

ENCODE Analysis of chromatin accessibility acrossbiosamples

We obtained the union set of DNase peak calls across 95 ENCODE biosamples using the "Table Browser" utility on the UCSC Genome Browser (downloaded February 2023; "wgEncodeRegDnaseClustered"). The union DNase peak calls were intersected with all regions included in the bulk screen library using bedtools intersect. Next, each region significant in at least one of two screens was labeled as "1" or "0" if the region did or did not overlap an accessible region in at least one biosample, respectively. The region X biosample visualization was generated using the pheatmap package in R with the following parameters: scale = "none", cluster_cols = TRUE, cluster_rows = TRUE. To extract the clusters, we used the cutree_col function specifying h=8. We then compared the phenotype scores between each cluster by performing One-way ANOVA tests followed by Tukey's post-hoc tests

using the aov and TukeyHSD functions in R.

To determine if significant screen regions were enriched or depleted from accessible regions in specific biosamples, we performed Fisher's exact tests separately for each biosample comparing the number of significant and nonsignificant screen regions that overlapped or did not overlap an accessible region using the fisher.test function in R.

Single cell RNA-seq screen

gRNA library design and cloning

Following hit identification from the combined migration and growth screens (as described above), a library was designed that included the top 10 gRNA by pZ value across either screen for the 87 hit pRE (870 gRNA total). 100 nontargeting control gRNA with similar sequence composition to the targeting gRNAs were included in the library, and 25 gRNA targeting the promoters of contractile genes including MYH9, RANGAPI, and CRIMI were included, as well as the top gRNA from the MYH9 intron 3 enhancer as positive controls. In total our library contained 1005 gRNA sequences, which were synthesized as an oligo pool by Twist Biosciences with common overhangs for cloning into our lentiviral backbone. This oligo pool was PCR amplified, and a hU6-driven lentiviral gRNA CROP-seq vector (Addgene Plasmid #106280) was then digested with Esp3I, gel purified, and then ligated along with the amplified oligo pool by Gibson assembly. Following a 1x SPRI cleaning, the Gibson assembly was transformed into Endura competent cells (Lucigen) according to the manufacturer's protocol, and cultured overnight before maxi-prepping the gRNA-library plasmid. A PCR amplicon across the gRNA region of the resulting plasmid was sequenced to a depth of ~100k-1M read pairs on an Illumina miSeg in order to verify coverage across the entire gRNA library (fig. S29).

Lentiviral generation and functional titering

First release: 25 September 2025

gRNA library plasmid was co-transfected into ~18M HEK293T cells along with two lentiviral packaging plasmids using Lipofectamine 3000 (ThermoFisher). 20 hours posttransfection, the growth media was removed and fresh growth media was added. Media containing viral particles was removed at 48 hours, replaced, and removed at 72 hours post-lipofection before being stored at 4C. Combined media containing viral particles was filtered through 0.45 µm lowprotein binding filters, and then concentrated using Lenti-X Concentrator (Takara Bio) according to the manufacturer's protocol. Functional titering to determine MOI was performed by transducing HFF cells across a 50x-10,000x dilution range of the viral stock, and then subjecting the cells to a qPCR-based titering protocol that has been previously described in detail (118).

Single cell CRISPRi screen

To perform screening, 775k HFF cells stably expressing dCas9-KRAB were transduced at 0.33MOI with the CROP-seq lentivirus to maintain a coverage of at least 150 cells/gRNA. Following 20 hours, viral media was removed and replaced with regular growth media, and 48 hours post-transduction the cells selected with puromycin (1.5 ug/mL) for 4 days. Following puromycin selection, HFF cells were maintained until day 8, at which point cells were trypsinized and 150k cells were moved on to library prep.

Single cell RNA-seq library preparation

Cells were washed 3x with PBS and then resuspended to a final concentration of 1000 cells/uL. Approximately 20,000 cells were loaded onto each channel of a 10X Genomics' 3' Gene Expression (GEX) v3.1 assay chip. Downstream processing was performed according to the manufacturer's protocol. To recover the protospacer sequences (gRNA libraries), a tri-nested PCR was performed separately for each GEX library using 10% of the purified cDNA as input to reaction 1 as previously described (29). Briefly, 4ng cDNA was input into a 50 uL reaction with KAPA HiFi and PCR primers prLRB470 and prLRB471 (table S22). The reaction was amplified for 12 cycles and then purified using 25 uL of AMPure XP DNA beads and eluted in 25 uL H20. 1 uL of the purified sample was input into reaction 2 using PCR primers prLRB472 and prLRB473 (table S22). The reaction was amplified for 14 cycles and purified as described above. 1 uL of the purified sample was input into reaction 3 using PCR primers prLRB473 and prLRB289-302 (table S22), amplifying each sample with a unique if acquiring index. The reaction was amplified for a unique if acquiring index. The reaction was amplified for second and prlr acquiring index. a unique i7 sequencing index. The reaction was amplified for 7 cycles, purified using 25 uL of AMPure XP DNA beads (Beckman Coulter #A63881), and eluted in 25 uL Buffer EB (Qiagen #19086). Quality control of final libraries was performed prior to sequencing using the Agilent 2200 TapeStation with High Sensitivity DNA 5000 reagents, Qubit High Sensitivity dsDNA reagents, and KAPA Library Quantification Kit for Illumina platforms.

Sequencing

GEX libraries were pooled and sequenced on a NovaSeq 6000 S4 flow cell using the parameters: 28x10x10x90. gRNA libraries were pooled and sequenced on a NovaSeq 6000 S1 flow cell using the parameters: 28x10x10x90.

Data processing

Cell Ranger: All data processing steps were performed using CellRanger v6.0.1 and the human reference genome ("refdatagex-GRCh38-2020-A") was downloaded from 10X Genomics' software downloads webpage. Fastq files for each flow cell lane and sequencing run were generated from .bcl files using the cellranger mkfastq pipeline. The corresponding fastq files for each sample were then merged. The merged fastqs were then processed using the cellranger count pipeline with the number of expected cells specified (--expect-cells = 15000). The gene expression libraries were then aggregated using the cellranger aggr pipeline. The gRNA libraries were aligned to a custom bowtie index containing all protospacer sequences included in the pooled gRNA library and the UMI counts corresponding to each gRNA-cell pair were obtained.

Seurat: The gene expression and gRNA UMI count data was imported into Seurat v3.1. A gRNA was defined as "observed in a cell" if the gRNA had at least 5 UMI counts and comprised at least 0.5% of the total gRNA UMI counts in that cell. We then calculated the total percent of mitochondrial reads per cell and filtered for quality cells as follows:

cells[["percent.mt"]] <- PercentageFeatureSet(cells, pat $tern = "^MT-"$

cells <- subset(cells, subset = nCount_RNA > 10000 & percent.mt < 20)

Differential expression analysis

Using the gRNA-cell assignments, differential expression testing was performed using the MAST framework (119) within Seurat v3.1 (120), comparing cells in which a given gRNA was observed versus all other cells with at least one gRNA observed excluding the given gRNA and testing all genes within ±1Mb of the midpoint of the pRE in which the gRNA is located. Gene coordinates were obtained from the Ensembl Human Gene v104 reference file. P-values were then FDR-corrected on an individual gRNA-level for all tests. All genes within ±1Mb of any targeting gRNA were used as input features for NT gRNA tests (N=1,313). Significant gRNA-gene and corresponding pRE-gene pairs are defined as FDR < 0.01.

Calculation of interaction distance (ep_length)

First release: 25 September 2025

The distance between the gRNA and the paired gene was calculated as follows: 1) the gRNA midpoint (gRNA_mid) was defined as (gRNA_start + gRNA_end)/2, the gene start coordinate (gene_start) was defined as the start coordinate for genes on the "+" plus strand, and end coordinate for genes on the "-" strand. "ep_length" was calculated as gRNA_mid gene start.

Effect size comparison between targeting and control gRNAs For each gene with a TSS- or validated enhancer-targeting gRNA, we compared the avg_logFC of expression for the respective gene between TSS-control, enhancer-control, pREtargeting, and NT-control gRNAs (FDR < 0.01), using a oneway ANOVA followed by Tukey's HSD with Bonferroni correction (adj. p-value). Significant differences in the change in gene expression were defined as adj. p-value < 0.05.

Interaction distance versus effect size

Using all significant pRE-targeting gRNA gene pairs, the avg_logFC and effect size (avg_logFC*(1-FDR)) were plotted versus the log10-transformed ep_length (log10(abs(ep_length+1))). Spearman correlation R² values were calculated using the "stat_cor" function from the "ggpubr" R package.

Nearest gene prediction analysis

For each potential pRE-gene pair, we calculated the number of genes "skipped" by the element to regulate the gene as follows. First, for the significant pRE-gene connections, we defined the start and end coordinates for a given element and the start and end coordinates, and strand, for the paired gene. Next, we counted the number of genes detected in the gene expression dataset for which the entire gene body was contained within the region between the element and the connected gene. We repeated this for all significant pRE-gene connections.

Comparison to microC looping

We obtained chromatin contact data (table S19) and intersected all targeted pREs, TSS regions (±1kb) of every gene and all genes for which a differential expression test was performed, separately extended by ±500bp with anchor 1 and anchor 2, using bedtools window -w 500. We then quantified the number of pREs, TSSs, and genes with at least one chromatin contact, defined as at least one intersection with anchor 1 or anchor 2. Next, for all regions that intersected a region in the anchor 1 set, we quantified the number of pREgene pairs for which the corresponding contact in the anchor 2 set overlapped either the same TSS/gene or a different TSS/gene. We repeated this for pREs intersecting the anchor 2 set with comparison of contacts for TSSs/genes in the anchor 1 set.

Comparison to ENCODE candidate cis-regulatory elements (cCREs) and chromHMM annotations

We obtained cCRE annotations from all human tissues and chromHMM annotations in human foreskin fibroblast primary cells (table S23). The cCREs and annotated regions were intersected with all regions included in the bulk screen and single cell screen libraries using bedtools intersect. To determine if significant screen regions were enriched or depleted from accessible regions in specific biosamples, we performed Fisher's exact tests comparing the number of significant and nonsignificant screen regions that overlapped or did not overlap an annotation using the fisher test function in R.

Single cell screen versus individual gRNA validations For the 10 pRE-gene connections with at least one significant individual gRNA validation, we calculated the Spearman

science.org

correlation (R2) and p-value between the change in mRNA expression measured via RT-qPCR (DDCt) versus the gene expression change observed in the single cell screen (avg_logFC of the most significant gRNA-gene connection per DHS) using the "stat_cor" function from the "ggpubr" R package.

Individual gRNA validations: HFF cells

Oligos containing protospacer sequences were synthesized by IDT and cloned into pLV hU6-sgRNA hUbC-GFP-P2A-PuroR (Addgene plasmid #162335). Sanger sequencing was used to confirm the identity of the gRNA. Lentivirus was generated as described above. dCas9-KRAB expressing HFF cells were seeded onto TCP and transduced on day 0. 24 hours post-transduction, lentivirus was removed. Antibiotic selection was applied and cells were harvested eight days posttransduction. mRNA was isolated using the Norgen Total RNA Purification Kit (#17250) according to the manufacturer's protocol. 100 ng mRNA was used as input for cDNA amplification using the Invitrogen SuperScript VILO cDNA Synthesis Kit. For RT-qPCR, each reaction contained 1 uL cDNA, 7 uL H20, 1 uL Taqman probe for TBP, 1 uL Taqman probe for gene of interest, and 10 uL Quantabio PerfeCTa FastMix II. Delta delta Ct analysis was performed in Microsoft Excel. Graphpad Prism was utilized to conduct oneway ANOVA tests followed by Tukey's HSD for post-hoc testing. Significance is reported in Fig.s as follows: *p-value < 0.05, **p-value < 0.01, ***p-value < 0.001. Taqman probe information is provided in table S16.

Individual gRNA validations: A549 / HFF cells

First release: 25 September 2025

Oligos containing protospacer sequences were synthesized by IDT and cloned into pLV_hU6-sgRNA_hUbC-GFP-P2A-PuroR (Addgene plasmid #162335). Sanger sequencing was used to confirm the identity of the gRNA. Lentivirus was generated as described above. dCas9-KRAB expressing A549/HFF cells were seeded onto TCP and transduced on day 0. 24 hours post-transduction, lentivirus was removed and replaced with fresh media. 2 days post-transduction, antibiotic selection was applied. 8 days post-transduction, cells were seeded on 24 well Matrigen dishes of varying stiffness (1 or 50 kPa elastic modulus) or TCP at slightly variable densities to account for reduced cell attachment on softer substrates (20,000 on 1 kPa and 12,500 on 50 kPa/TCP for A549 and 30,000 on 1 kPa and 18,750 on 50 kPa/TCP) and allowed to culture for 20 hours overnight. mRNA was isolated using the Norgen Total RNA Purification Kit (#17250) according to the manufacturer's protocol. 100 ng mRNA was used as input for cDNA amplification using the Invitrogen SuperScript VILO cDNA Synthesis Kit. For RT-qPCR, each reaction contained 1 uL cDNA, 7 uL H20, 0.5 uL Taqman probe for TBP, 0.5 uL Taqman probe for gene of interest, and 10 uL Quantabio PerfeCTa FastMix II. Delta delta Ct analysis was performed in

Microsoft Excel. Graphpad Prism was utilized to conduct oneway ANOVA tests followed by Tukey's HSD for post-hoc testing. Significance is reported in Fig.s as follows: *p-value < 0.05, **p-value < 0.01, ***p-value < 0.001. Tagman probe information is provided in table S20.

Patient derived lung fibroblast isolations validations

Human lung tissue dissociation

Human lung dissociation was performed as described previously (121). Briefly, approximately 2-3 g of human lung tissue was washed with PBS containing 1% Antibiotic-Antimycotic followed by removal of pleura, small airway and visible vasculature. Remaining tissue was cut into small pieces followed by incubation with enzyme mixture (Collagenase type I: 1.68) mg/ml, Dispase: 5U/ml, DNase: 10U/ml) at 37°C for 1-1.5 hours with rotation. The cells were filtered through a $100\mu m$ strainer and rinsed with DMEM containing 10% FBS. Cell suspension was spun down at 450 g for 10 min and the cell pellet was resuspended in red blood cell lysis buffer for 5min. washed with DMEM containing 10% FBS and filtered through a 40µm strainer. Total cells were centrifuged at 450 g for 5 min at 4°C and the cell pellet was used for isolation of fibroblasts.

Primary human fibroblasts enrichment by MACS

Fibroblast enrichment was done using magnetic activated cell sorting (MACS) as previously described (122). Briefly, following lung dissociation, cells were incubated in MACS buffer (1% BSA, 2mM EDTA, antibiotic/antimycotic in PBS, pH 7.2) containing CD146 (Miltenvi Biotec 130-093-596, 1:50). CD45 (Miltenyi Biotec 130-045-801, 1:50), and CD326 (Miltenyi Biotec 130-061-101, 1:50) microbeads at 4°C for one hour with rotation. Cells were then washed and incubated with CD31 biotinylated antibody (Miltenyi Biotec, 130-110-805, 1:50) at 4°C for 10 min followed by washes and incubation with streptavidin microbeads (Miltenyi Biotec, 130-048-102, 1:10) at 4°C for 15 min. Magnetic separation of antibody bound cells was performed using Miltenyi Biotec LS columns (130-042-401). Fibroblasts collected from the flowthrough were resuspended in fibroblast growth media (advanced DMEM/F12, Antibiotic/Antimycotic (Gibco 15240062, 100X). HEPES (Thermo Fisher Scientific, 15630080), GlutaMAX (Thermo Fisher Scientific, 35050061), B27 supplement (Thermo Fisher Scientific, 17504044), N2 supplement (Thermo Fisher Scientific, 17502048), N-acetylcysteine (Sigma-Aldrich, A9165) and 10ng/mL PDGFα (Biolegend 773708), plated cultured on 5% Matrigel (Corning 354230) coated dish. Media was changed every 2-3 days.

Primary human fibroblast culture and viral transduction To facilitate gene loss of function, fibroblasts were first

transduced with lentivirus (1:50) containing dCas9-KRAB. Medium was changed 24 hours post transduction followed treatment with 8ug/mL blasticidin for 5 days. Blasticidin-selected fibroblasts were then grown in fibroblast growth media without blasticidin for 24 hours, trypsinized, and replated in a 24 well plate. Fibroblasts were then transduced with one of the following lentiviruses (1:100): Skp2 gRNA, CCN1 gRNA, CCN2 gRNA, Mint3 gRNA, or Non-targeting control. Medium was changed 24 hours after transduction, and fibroblasts were grown for one day in fibroblast growth media followed by treatment with 0.5 ug/mL puromycin for 3 days. After selection, the media was changed to either standard fibroblast growth media, or fibroblast growth media supplemented with 10ng/mL hTGF\$1 (Biolegend 580702). Cells were collected for RNA isolation on day 5.

Immunofluorescence staining of primary human fibroblasts Fibroblasts were fixed in 4% paraformaldehyde for 15 min at room temperature. Samples were washed three times with PBS, permeabilized with PBST (0.1%Triton-X 100 in PBS) followed by blocking and incubation with primary antibodies: PDGFRA (R&D Systems, AF-307-SP, 1:500), Ki67 (eBioscience 14-5698-82, 1:500), and αSMA-cy3 (Sigma-Aldrich C6198, 1:500) overnight at 4°C with. Fibroblasts were washed 3 times with PBST and incubated with the following secondary antibodies: Donkey-anti-goat IgG Alexa Fluor 647 (Invitrogen A-21447, 1:500) and donkey-anti-rat IgG Alexa Fluor 488 (Invitrogen A-21208, 1:500) for one hour. Samples were then washed three times with PBST, once with PBST containing DAPI followed by one wash in PBST. Confocal images were captured using Olympus FV3000 microscope with 10X objective.

Human lung specimens

See Tables 1 and 2 for descriptions of healthy and IPF donors, respectively.

REFERENCES AND NOTES

First release: 25 September 2025

- 1. S. J. Morrison, A. C. Spradling, Stem cells and niches: Mechanisms that promote stem cell maintenance throughout life. Cell 132, 598-611 (2008). doi:10.1016/i.cell.2008.01.038 Medline
- 2. D. L. Jones, A. J. Wagers, No place like home: Anatomy and function of the stem cell niche. Nat. Rev. Mol. Cell Biol. 9, 11-21 (2008). doi:10.1038/nrm2319 Medline
- 3. P. Jiang, Y. Zhang, B. Ru, Y. Yang, T. Vu, R. Paul, A. Mirza, G. Altan-Bonnet, L. Liu, E. Ruppin, L. Wakefield, K. W. Wucherpfennig, Systematic investigation of cytokine signaling activity at the tissue and single-cell levels. Nat. Methods 18, 1181–1191 (2021). doi:10.1038/s41592-021-01274-5 Medline
- 4. D. R. Simeonov, B. G. Gowen, M. Boontanrart, T. L. Roth, J. D. Gagnon, M. R. Mumbach, A. T. Satpathy, Y. Lee, N. L. Bray, A. Y. Chan, D. S. Lituiev, M. L. Nguyen, R. E. Gate, M. Subramaniam, Z. Li, J. M. Woo, T. Mitros, G. J. Ray, G. L. Curie, N. Naddaf, J. S. Chu, H. Ma, E. Boyer, F. Van Gool, H. Huang, R. Liu, V. R. Tobin, K. Schumann, M. J. Daly, K. K. Farh, K. M. Ansel, C. J. Ye, W. J. Greenleaf, M. S. Anderson, J. A. Bluestone, H. Y. Chang, J. E. Corn, A. Marson, Discovery of stimulation-responsive immune enhancers with CRISPR activation. Nature 549, 111-115 (2017). doi:10.1038/nature23875 Medline

- 5. G. Korkmaz, R. Lopes, A. P. Ugalde, E. Nevedomskaya, R. Han, K. Myacheva, W. Zwart, R. Elkon, R. Agami, Functional genetic screens for enhancer elements in the human genome using CRISPR-Cas9. Nat. Biotechnol. 34, 192-198 (2016). doi:10.1038/nbt.3450 Medline
- 6. K. Han, S. E. Pierce, A. Li, K. Spees, G. R. Anderson, J. A. Seoane, Y.-H. Lo, M. Dubreuil, M. Olivas, R. A. Kamber, M. Wainberg, K. Kostyrko, M. R. Kelly, M. Yousefi, S. W. Simpkins, D. Yao, K. Lee, C. J. Kuo, P. K. Jackson, A. Sweet-Cordero, A. Kundaje, A. J. Gentles, C. Curtis, M. M. Winslow, M. C. Bassik, CRISPR screens in cancer spheroids identify 3D growth-specific vulnerabilities. Nature 580, 136-141 (2020). doi:10.1038/s41586-020-2099-x Medline
- 7. R. McBeath, D. M. Pirone, C. M. Nelson, K. Bhadriraju, C. S. Chen, Cell shape, cytoskeletal tension, and RhoA regulate stem cell lineage commitment. Dev. Cell 6, 483-495 (2004). doi:10.1016/S1534-5807(04)00075-9 Medline
- 8. C. S. Chen, M. Mrksich, S. Huang, G. M. Whitesides, D. E. Ingber, Geometric control life and death. Science 276, 1425-1428 doi:10.1126/science.276.5317.1425 Medline
- 9. A. J. Engler, S. Sen, H. L. Sweeney, D. E. Discher, Matrix elasticity directs stem cell lineage specification. Cell 126, 677-689 (2006). doi:10.1016/i.cell.2006.06.044 Medline
- 10. R. J. Pelham Jr., Y. Wang, Cell locomotion and focal adhesions are regulated by substrate flexibility. Proc. Natl. Acad. Sci. U.S.A. 94, 13661-13665 (1997). doi:10.1073/pnas.94.25.13661.Medline
- 11. S. Dupont, S. A. Wickström, Mechanical regulation of chromatin and transcription. Nat. Rev. Genet. 23, 624-643 (2022). doi:10.1038/s41576-022-00493-6 Medline
- 12. S. Piccolo, S. Dupont, M. Cordenonsi, The biology of YAP/TAZ: Hippo signaling and beyond. Physiol. Rev. 94, 1287-1312 (2014). doi:10.1152/physrev.00005.2
- 13. S. Dupont, L. Morsut, M. Aragona, E. Enzo, S. Giulitti, M. Cordenonsi, F. Zanconato, J. Le Digabel, M. Forcato, S. Bicciato, N. Elvassore, S. Piccolo, Role of YAP/TAZ in mechanotransduction. Nature 474, 179-183 (2011). doi:10.1038/nature10137
- 14. Z. Meng, Y. Qiu, K. C. Lin, A. Kumar, J. K. Placone, C. Fang, K.-C. Wang, S. Lu, M. Pan, A. W. Hong, T. Moroishi, M. Luo, S. W. Plouffe, Y. Diao, Z. Ye, H. W. Park, X. Wang, F.-X. Yu, S. Chien, C.-Y. Wang, B. Ren, A. J. Engler, K.-L. Guan, RAP2 mediates mechanoresponses of the Hippo pathway. Nature 560, 655-660 (2018). doi:10.1038/s41586-018-0444-0 Medline
- 15. F. R. Bischoff, C. Klebe, J. Kretschmer, A. Wittinghofer, H. Ponstingl, RanGAP1 induces GTPase activity of nuclear Ras-related Ran. Proc. Natl. Acad. Sci. U.S.A. 91, 2587-2591 (1994). doi:10.1073/pnas.91.7.2587 Medline
- 16. C. Y. Ho, D. E. Jaalouk, M. K. Vartiainen, J. Lammerding, Lamin A/C and emerin regulate MKL1-SRF activity by modulating actin dynamics. Nature 497, 507-511 (2013). doi:10.1038/nature12105 Medline
- 17. M. K. Vartiainen, S. Guettler, B. Larijani, R. Treisman, Nuclear actin regulates dynamic subcellular localization and activity of the SRF cofactor MAL. Science 316, 1749-1752 (2007). doi:10.1126/science.1141084 Medline
- 18. F. Miralles, G. Posern, A.-l. Zaromytidou, R. Treisman, Actin dynamics control SRF activity by regulation of its coactivator MAL. Cell 113, 329-342 (2003). doi:10.1016/S0092-8674(03)00278-2 Medline
- 19. Y. A. Miroshnikova, M. M. Nava, S. A. Wickström, Emerging roles of mechanical forces in chromatin regulation. J. Cell Sci. 130, 2243-2250 (2017). doi:10.1242/ics.202192 Medline
- 20. H. Q. Le, S. Ghatak, C.-Y. C. Yeung, F. Tellkamp, C. Günschmann, C. Dieterich, A. Yeroslaviz, B. Habermann, A. Pombo, C. M. Niessen, S. A. Wickström, Mechanical regulation of transcription controls Polycomb-mediated gene silencing during lineage commitment. Nat. Cell Biol. 18, 864-875 (2016). doi:10.1038/ncb3387 Medline
- 21. S.-J. Heo, T. P. Driscoll, S. D. Thorpe, N. L. Nerurkar, B. M. Baker, M. T. Yang, C. S. Chen, D. A. Lee, R. L. Mauck, Differentiation alters stem cell nuclear architecture, mechano-sensitivity. mechanics. and eLife doi:10.7554/eLife.18207 Medline
- 22. M. M. Nava, Y. A. Miroshnikova, L. C. Biggs, D. B. Whitefield, F. Metge, J. Boucas, H. Vihinen, E. Jokitalo, X. Li, J. M. García Arcos, B. Hoffmann, R. Merkel, C. M. Niessen, K. N. Dahl, S. A. Wickström, Heterochromatin-driven nuclear softening protects the genome against mechanical stress-induced damage. Cell 181, 800-817.e22 (2020). doi:10.1016/j.cell.2020.03.052 Medline

- 23. A. Tajik, Y. Zhang, F. Wei, J. Sun, Q. Jia, W. Zhou, R. Singh, N. Khanna, A. S. Belmont, N. Wang, Transcription upregulation via force-induced direct stretching of chromatin. Nat. Mater. 15, 1287-1296 (2016). doi:10.1038/nmat4729 Medline
- 24. J. Sun, J. Chen, E. Mohagheghian, N. Wang, Force-induced gene up-regulation does not follow the weak power law but depends on H3K9 demethylation. Sci. Adv. 6, eaay9095 (2020). doi:10.1126/sciadv.aay9095 Medline
- 25. ENCODE Project Consortium, An integrated encyclopedia of DNA elements in the human genome. Nature 489, 57-74 (2012). doi:10.1038/nature11247 Medline
- 26. F. Zanconato, M. Forcato, G. Battilana, L. Azzolin, E. Quaranta, B. Bodega, A. Rosato, S. Bicciato, M. Cordenonsi, S. Piccolo, Genome-wide association between YAP/TAZ/TEAD and AP-1 at enhancers drives oncogenic growth. Nat. Cell Biol. 17, 1218-1227 (2015). doi:10.1038/ncb3216 Medline
- 27. G. G. Galli, M. Carrara, W.-C. Yuan, C. Valdes-Quezada, B. Gurung, B. Pepe-Mooney, T. Zhang, G. Geeven, N. S. Gray, W. de Laat, R. A. Calogero, F. D. Camargo, YAP drives growth by controlling transcriptional pause release from enhancers. Mol. Cell 60. 328-337 (2015).doi:10.1016/i.molcel.2015.09.001 Medline
- 28. J. P. Noonan, A. S. McCallion, Genomics of long-range regulatory elements. Annu. Rev. Genomics Hum. Genet. 11, 1-23 (2010). doi:10.1146/annurev-genom-082509-141651 Medline
- 29. M. Gasperini, A. J. Hill, J. L. McFaline-Figueroa, B. Martin, S. Kim, M. D. Zhang, D. Jackson, A. Leith, J. Schreiber, W. S. Noble, C. Trapnell, N. Ahituv, J. Shendure, A. genome-wide framework for mapping gene regulation via cellular genetic screens. Cell 176, 377-390.e19 (2019). doi:10.1016/j.cell.2018.11.029 Medline
- 30. T. S. Klann, J. B. Black, M. Chellappan, A. Safi, L. Song, I. B. Hilton, G. E. Crawford, T. E. Reddy, C. A. Gersbach, CRISPR-Cas9 epigenome editing enables highthroughput screening for functional regulatory elements in the human genome. Nat. Biotechnol. 35, 561-568 (2017). doi:10.1038/nbt.3853 Medline
- 31. M. V. Plikus, X. Wang, S. Sinha, E. Forte, S. M. Thompson, E. L. Herzog, R. R. Driskell, N. Rosenthal, J. Biernaskie, V. Horsley, Fibroblasts: Origins, definitions, and functions in health and disease. Cell 184, 3852-3872 (2021). doi:10.1016/i.cell.2021.06.024 Medline
- 32. J. Swift, I. L. Ivanovska, A. Buxboim, T. Harada, P. C. D. P. Dingal, J. Pinter, J. D. Pajerowski, K. R. Spinler, J.-W. Shin, M. Tewari, F. Rehfeldt, D. W. Speicher, D. E. Discher, Nuclear lamin-A scales with tissue stiffness and enhances matrixdirected differentiation 341. 1240104 Science (2013).doi:10.1126 science.1240104 Medline
- 33. P. Song, J.-X. Zheng, J. Xu, J.-Z. Liu, L.-Y. Wu, C. Liu, β-catenin induces A549 alveolar epithelial cell mesenchymal transition during pulmonary fibrosis. Mol. Med. Rep. 11, 2703-2710 (2015). doi:10.3892/mmr.2014.3013 Medline
- 34. D. Zhao, C. Xue, Q. Li, M. Liu, W. Ma, T. Zhou, Y. Lin, Substrate stiffness regulated migration and angiogenesis potential of A549 cells and HUVECs. J. Cell. Physiol. 233, 3407-3417 (2018). doi:10.1002/jcp.26189 Medline
- 35. I. C. McDowell, A. Barrera, A. M. D'Ippolito, C. M. Vockley, L. K. Hong, S. M. Leichter, L. C. Bartelt, W. H. Majoros, L. Song, A. Safi, D. D. Koçak, C. A. Gersbach, A. J. Hartemink, G. E. Crawford, B. E. Engelhardt, T. E. Reddy, Glucocorticoid receptor recruits to enhancers and drives activation by motif-directed binding. Genome Res. 28, 1272-1284 (2018). doi:10.1101/gr.233346.117 Medline
- 36. V. F. Achterberg, L. Buscemi, H. Diekmann, J. Smith-Clerc, H. Schwengler, J.-J. Meister, H. Wenck, S. Gallinat, B. Hinz, The nano-scale mechanical properties of the extracellular matrix regulate dermal fibroblast function. J. Invest. Dermatol. 134, 1862–1872 (2014). doi:10.1038/jid.2014.90 Medline
- 37. K. Arda, N. Ciledag, E. Aktas, B. K. Aribas, K. Köse, Quantitative assessment of normal soft-tissue elasticity using shear-wave ultrasound elastography. AJR Am. J. Roentgenol. 197, 532-536 (2011). doi:10.2214/AJR.10.5449 Medline
- 38. C. X. Li, N. P. Talele, S. Boo, A. Koehler, E. Knee-Walden, J. L. Balestrini, P. Speight, A. Kapus, B. Hinz, MicroRNA-21 preserves the fibrotic mechanical memory of mesenchymal stem cells. Nat. Mater. 16, 379-389 (2017). doi:10.1038/nmat4780
- 39. M. Darnell, L. Gu, D. Mooney, RNA-seq reveals diverse effects of substrate stiffness on mesenchymal stem cells. Biomaterials 181, 182-188 (2018). doi:10.1016/j.biomaterials.2018.07.039 Medline
- 40. D. L. Jones, G. F. Hallström, X. Jiang, R. C. Locke, M. K. Evans, E. D. Bonnevie, A. Srikumar, T. P. Leahy, M. P. Nijsure, J. D. Boerckel, R. L. Mauck, N. A. Dyment, Mechanoepigenetic regulation of extracellular matrix homeostasis via Yap and

- Taz. Proc. Natl. Acad. Sci. U.S.A. 120. e2211947120 (2023).doi:10.1073/pnas.2211947120 Medline
- 41. S. Heinz, C. E. Romanoski, C. Benner, C. K. Glass, The selection and function of cell type-specific enhancers. Nat. Rev. Mol. Cell Biol. 16, 144-154 (2015). doi:10.1038/nrm3949 Medline
- 42. Y. Liu-Chittenden, B. Huang, J. S. Shim, Q. Chen, S.-J. Lee, R. A. Anders, J. O. Liu, D. Pan, Genetic and pharmacological disruption of the TEAD-YAP complex suppresses the oncogenic activity of YAP. Genes Dev. 26, 1300-1305 (2012). doi:10.1101/gad.192856.112 Medline
- 43. E. M. Lisabeth, D. Kahl, I. Gopallawa, S. E. Haynes, S. A. Misek, P. L. Campbell, T. S. Dexheimer, D. Khanna, D. A. Fox, X. Jin, B. R. Martin, S. D. Larsen, R. R. Neubig, Identification of pirin as a molecular target of the CCG-1423/CCG-203971 series of antifibrotic and antimetastatic compounds. ACS Pharmacol. Transl. Sci. 2, 92-100 (2019). doi:10.1021/acsptsci.8b00048 Medline
- 44. M. Bentsen, P. Goymann, H. Schultheis, K. Klee, A. Petrova, R. Wiegandt, A. Fust, J. Preussner, C. Kuenne, T. Braun, J. Kim, M. Looso, ATAC-seq footprinting unravels kinetics of transcription factor binding during zygotic genome activation. Nat. Commun. 11, 4267 (2020). doi:10.1038/s41467-020-18035-1 Medline
- 45. R. S. Stowers, A. Shcherbina, J. Israeli, J. J. Gruber, J. Chang, S. Nam, A. Rabiee, M. N. Teruel, M. P. Snyder, A. Kundaje, O. Chaudhuri, Matrix stiffness induces a tumorigenic phenotype in mammary epithelium through changes in chromatin accessibility. Nat. Biomed. Eng. 3, 1009-1019 (2019). doi:10.1038/s41551-019-0420-5 Medline
- 46. J. M. Miano, Serum response factor: Toggling between disparate programs of gene expression. J. Mol. Cell. Cardiol. 35, 577-593 (2003). doi:10.1016/S0022-2828(03)00110-X Medline
- 47. D. L. Jones, J. A. Meridew, P. A. Link, M. T. Ducharme, K. L. Lydon, K. M. Choi, N. Caporarello, Q. Tan, A. M. Diaz Espinosa, Y. Xiong, J.-H. Lee, Z. Ye, H. Yan, T. Ordog, G. Ligresti, X. Varelas, D. J. Tschumperlin, ZNF416 is a pivotal transcriptional regulator of fibroblast mechanoactivation. J. Cell Biol. 220, e202007152 (2021). doi:10.1083/icb.202007152 Medline
- 48. M. Vicente-Manzanares, X. Ma, R. S. Adelstein, A. R. Horwitz, Non-muscle myosin Il takes centre stage in cell adhesion and migration. Nat. Rev. Mol. Cell Biol. 10, 778-790 (2009). doi:10.1038/nrm2786 Medline
- 49. P. I. Thakore, A. M. D'Ippolito, L. Song, A. Safi, N. K. Shivakumar, A. M. Kabadi, T. E. Reddy, G. E. Crawford, C. A. Gersbach, Highly specific epigenome editing by CRISPR-Cas9 repressors for silencing of distal regulatory elements. Nat. Methods 12, 1143–1149 (2015). doi:10.1038/nmeth.3630 Medline
- 50. L. A. Gilbert, M. H. Larson, L. Morsut, Z. Liu, G. A. Brar, S. E. Torres, N. Stern-Ginossar, O. Brandman, E. H. Whitehead, J. A. Doudna, W. A. Lim, J. S. Weissman, L. S. Qi, CRISPR-mediated modular RNA-guided regulation of transcription in eukaryotes. Cell 154, 442-451 (2013). doi:10.1016/i.cell.2013.06.044 Medline
- 51. B. D. Hoffman, C. Grashoff, M. A. Schwartz, Dynamic molecular processes mediate mechanotransduction. 475. 316-323 (2011).Nature doi:10.1038/nature10316 Medline
- 52. M. C. Canver, E. C. Smith, F. Sher, L. Pinello, N. E. Sanjana, O. Shalem, D. D. Chen, P. G. Schupp, D. S. Vinjamur, S. P. Garcia, S. Luc, R. Kurita, Y. Nakamura, Y. Fujiwara, T. Maeda, G.-C. Yuan, F. Zhang, S. H. Orkin, D. E. Bauer, BCL11A enhancer dissection by Cas9-mediated in situ saturating mutagenesis. Nature 527, 192–197 (2015). doi:10.1038/nature15521 Medline
- 53. L. Chang, L. Azzolin, D. Di Biagio, F. Zanconato, G. Battilana, R. Lucon Xiccato, M. Aragona, S. Giulitti, T. Panciera, A. Gandin, G. Sigismondo, J. Krijgsveld, M. Fassan, G. Brusatin, M. Cordenonsi, S. Piccolo, The SWI/SNF complex is a mechanoregulated inhibitor of YAP and TAZ. Nature 563, 265-269 (2018). doi:10.1038/s41586-018-0658-1 Medline
- 54. J. Oliver-De La Cruz, G. Nardone, J. Vrbsky, A. Pompeiano, A. R. Perestrelo, F. Capradossi, K. Melajová, P. Filipensky, G. Forte, Substrate mechanics controls adipogenesis through YAP phosphorylation by dictating cell spreading. Biomaterials 205, 64-80 (2019). doi:10.1016/j.biomaterials.2019.03.009 Medline
- 55. J. L. Leight, M. A. Wozniak, S. Chen, M. L. Lynch, C. S. Chen, Matrix rigidity regulates a switch between TGF-β1-induced apoptosis and epithelialmesenchymal transition. Mol. Biol. Cell 23, 781-791 (2012). doi:10.1091/mbc.e11-06-0537 Medline
- 56. Z. Ma, Z. Liu, D. P. Myers, L. S. Terada, Mechanotransduction and anoikis: Death

- and the homeless cell. Cell Cycle 7, 2462–2465 (2008). doi:10.4161/cc.7.16.6463
- 57. B. Zhao, L. Li, L. Wang, C.-Y. Wang, J. Yu, K.-L. Guan, Cell detachment activates the Hippo pathway via cytoskeleton reorganization to induce anoikis. Genes Dev. 26, 54-68 (2012). doi:10.1101/gad.173435.111 Medline
- 58. P. Paoli, E. Giannoni, P. Chiarugi, Anoikis molecular pathways and its role in cancer progression. Biochim. Biophys. Acta 1833, 3481-3498 doi:10.1016/i.bbamcr.2013.06.026 Medline
- 59. T. Schmelzle, A. A. Mailleux, M. Overholtzer, J. S. Carroll, N. L. Solimini, E. S. Lightcap, O. P. Veiby, J. S. Brugge, Functional role and oncogene-regulated expression of the BH3-only factor Bmf in mammary epithelial anoikis and morphogenesis. Proc. Natl. Acad. Sci. U.S.A. 104, 3787-3792 (2007). doi:10.1073/pnas.0700115104 Medline
- 60. M. Seo, S. Lee, J.-H. Kim, W.-H. Lee, G. Hu, S. J. Elledge, K. Suk, RNAi-based functional selection identifies novel cell migration determinants dependent on PI3K and AKT pathways. Nat. Commun. 5, 5217 (2014). doi:10.1038/ncomms6217
- 61. R. M. Meyers, J. G. Bryan, J. M. McFarland, B. A. Weir, A. E. Sizemore, H. Xu, N. V. Dharia, P. G. Montgomery, G. S. Cowley, S. Pantel, A. Goodale, Y. Lee, L. D. Ali, G. Jiang, R. Lubonja, W. F. Harrington, M. Strickland, T. Wu, D. C. Hawes, V. A. Zhivich, M. R. Wyatt, Z. Kalani, J. J. Chang, M. Okamoto, K. Stegmaier, T. R. Golub, J. S. Boehm, F. Vazquez, D. E. Root, W. C. Hahn, A. Tsherniak, Computational correction of copy number effect improves specificity of CRISPR-Cas9 essentiality screens in cancer cells. Nat. Genet. 49, 1779-1784 (2017). doi:10.1038/ng.3984 Medline
- 62. F. M. Behan, F. Iorio, G. Picco, E. Goncalves, C. M. Beaver, G. Migliardi, R. Santos, Y. Rao, F. Sassi, M. Pinnelli, R. Ansari, S. Harper, D. A. Jackson, R. McRae, R. Pooley, P. Wilkinson, D. van der Meer, D. Dow, C. Buser-Doepner, A. Bertotti, L. Trusolino, E. A. Stronach, J. Saez-Rodriguez, K. Yusa, M. J. Garnett, Prioritization of cancer therapeutic targets using CRISPR-Cas9 screens. Nature 568, 511-516 (2019). doi:10.1038/s41586-019-1103-9 Medline
- 63. H. Zhang, Y. Wang, W. Zhang, Q. Wu, J. Fan, Q. Zhan, BAALC-AS1/G3BP2/c-Myc feedback loop promotes cell proliferation in esophageal squamous cell 240-257 carcinoma. Cancer Commun. (Lond.) (2021).doi:10.1002/cac2.12127 Medline
- 64. C. Paulmann, R. Spallek, O. Karpiuk, M. Heider, I. Schäffer, J. Zecha, S. Klaeger, M. Walzik, R. Öllinger, T. Engleitner, M. Wirth, U. Keller, J. Krönke, M. Rudelius, S. Kossatz, R. Rad, B. Kuster, F. Bassermann, The OTUD6B-LIN28B-MYC axis determines the proliferative state in multiple myeloma. EMBO J. 41, e110871 (2022). doi:10.15252/embj.2022110871 Medline
- 65. M. Sun, G. Chi, P. Li, S. Lv, J. Xu, Z. Xu, Y. Xia, Y. Tan, J. Xu, L. Li, Y. Li, Effects of matrix stiffness on the morphology, adhesion, proliferation and osteogenic differentiation of mesenchymal stem cells. Int. J. Med. Sci. 15, 257-268 (2018). doi:10.7150/ijms.21620 Medline
- 66. M. Ehrbar, A. Sala, P. Lienemann, A. Ranga, K. Mosiewicz, A. Bittermann, S. C. Rizzi, F. E. Weber, M. P. Lutolf, Elucidating the role of matrix stiffness in 3D cell migration and remodeling. Biophys. J. 100, 284-293 (2011). doi:10.1016/i.bpi.2010.11.082 Medline
- 67. B. Mifsud, F. Tavares-Cadete, A. N. Young, R. Sugar, S. Schoenfelder, L. Ferreira, S. W. Wingett, S. Andrews, W. Grey, P. A. Ewels, B. Herman, S. Happe, A. Higgs, E. LeProust, G. A. Follows, P. Fraser, N. M. Luscombe, C. S. Osborne, Mapping longrange promoter contacts in human cells with high-resolution capture Hi-C. Nat. Genet. 47, 598-606 (2015), doi:10.1038/ng.3286 Medline
- 68. A. Sanyal, B. R. Lajoie, G. Jain, J. Dekker, The long-range interaction landscape of gene promoters. Nature 489, 109-113 (2012). doi:10.1038/nature11279 Medline
- 69. C. P. Fulco, J. Nasser, T. R. Jones, G. Munson, D. T. Bergman, V. Subramanian, S. R. Grossman, R. Anyoha, B. R. Doughty, T. A. Patwardhan, T. H. Nguyen, M. Kane, E. M. Perez, N. C. Durand, C. A. Lareau, E. K. Stamenova, E. L. Aiden, E. S. Lander, J. M. Engreitz, Activity-by-contact model of enhancer-promoter regulation from thousands of CRISPR perturbations. Nat. Genet. 51, 1664-1669 (2019). doi:10.1038/s41588-019-0538-0 Medline
- 70. J. E. Moore, M. J. Purcaro, H. E. Pratt, C. B. Epstein, N. Shoresh, J. Adrian, T. Kawli, C. A. Davis, A. Dobin, R. Kaul, J. Halow, E. L. Van Nostrand, P. Freese, D. U. Gorkin, Y. Shen, Y. He, M. Mackiewicz, F. Pauli-Behn, B. A. Williams, A. Mortazavi, C. A. Keller, X. O. Zhang, S. I. Elhajjajy, J. Huey, D. E. Dickel, V. Snetkova, X. Wei, X. Wang,

First release: 25 September 2025

- J. C. Rivera-Mulia, J. Rozowsky, J. Zhang, S. B. Chhetri, J. Zhang, A. Victorsen, K. P. White, A. Visel, G. W. Yeo, C. B. Burge, E. Lécuyer, D. M. Gilbert, J. Dekker, J. Rinn, E. M. Mendenhall, J. R. Ecker, M. Kellis, R. J. Klein, W. S. Noble, A. Kundaje, R. Guigó, P. J. Farnham, J. M. Cherry, R. M. Myers, B. Ren, B. R. Graveley, M. B. Gerstein, L. A. Pennacchio, M. P. Snyder, B. E. Bernstein, B. Wold, R. C. Hardison, T. R. Gingeras, J. A. Stamatoyannopoulos, Z. Weng; ENCODE Project Consortium, Expanded encyclopaedias of DNA elements in the human and mouse genomes. Nature 583, 699-710 (2020). doi:10.1038/s41586-020-2493-4 Medline
- 71. J. Ernst, M. Kellis, ChromHMM: Automating chromatin-state discovery and characterization. Nat. Methods 9, 215-216 (2012). doi:10.1038/nmeth.1906
- 72. A. M. Babic, M. L. Kireeva, T. V. Kolesnikova, L. F. Lau, CYR61, a product of a growth factor-inducible immediate early gene, promotes angiogenesis and tumor growth. Proc. Natl. Acad. Sci. U.S.A. 95, 6355-6360 (1998). doi:10.1073/pnas.95.11.6355 Medline
- 73. Z. Chen, N. Zhang, H. Y. Chu, Y. Yu, Z.-K. Zhang, G. Zhang, B.-T. Zhang, Connective Tissue growth factor: From molecular understandings to drug discovery. Front. Cell Dev. Biol. 8, 593269 (2020). doi:10.3389/fcell.2020.593269 Medline
- 74. F. Zhang, F. Hao, D. An, L. Zeng, Y. Wang, X. Xu, M.-Z. Cui, The matricellular protein Cyr61 is a key mediator of platelet-derived growth factor-induced cell migration. J. Biol. Chem. **290**, 8232–8242 (2015). <u>doi:10.1074/jbc.M114.623074 Medline</u>
- 75. W. I. Effendi, T. Nagano, Connective tissue growth factor in idiopathic pulmonary fibrosis: Breaking the bridge. Int. J. Mol. Sci. 23, 6064 (2022). doi:10.3390/ijms23116064 Medline
- 76. M. Mikamo, K. Kitagawa, S. Sakai, C. Uchida, T. Ohhata, K. Nishimoto, H. Niida, S. Suzuki, K. I. Nakayama, N. Inui, T. Suda, M. Kitagawa, Inhibiting Skp2 E3 ligase suppresses bleomycin-induced pulmonary fibrosis. Int. J. Mol. Sci. 19, 474 (2018). doi:10.3390/iims19020474 Medline
- 77. X. Sun, M. Zhu, X. Chen, X. Jiang, MYH9 inhibition suppresses TGF-β1-stimulated lung fibroblast-to-myofibroblast differentiation. Front. Pharmacol. 11, 573524 (2021). doi:10.3389/fphar.2020.573524 Medline
- 78. M. A. T. Freeberg, A. Perelas, J. K. Rebman, R. P. Phipps, T. H. Thatcher, P. J. Sime, Mechanical feed-forward loops contribute to idiopathic pulmonary fibrosis. Am. J. Pathol. 191, 18-25 (2021). doi:10.1016/i.aipath.2020.09.008 Medline
- 79. J. T. Allen, M. A. Spiteri, Growth factors in idiopathic pulmonary fibrosis: Relative roles. Respir. Res. 3, 13 (2002). doi:10.1186/rr162 Medline
- 80. H. N. Antoniades, M. A. Bravo, R. E. Avila, T. Galanopoulos, J. Neville-Golden, M. Maxwell, M. Selman, Platelet-derived growth factor in idiopathic pulmonary fibrosis. J. Clin. Invest. 86, 1055-1064 (1990). doi:10.1172/JCI114808 Medline
- 81. F. S. Younesi, A. E. Miller, T. H. Barker, F. M. V. Rossi, B. Hinz, Fibroblast and myofibroblast activation in normal tissue repair and fibrosis. Nat. Rev. Mol. Cell Biol. 25, 617-638 (2024). doi:10.1038/s41580-024-00716-0 Medline
- 82. J. Sun, Y. Guo, T. Chen, T. Jin, L. Ma, L. Ai, J. Guo, Z. Niu, R. Yang, Q. Wang, X. Yu, H. Gao, Y. Zhang, W. Su, X. Song, W. Ji, Q. Zhang, M. Huang, X. Fan, Z. Du, H. Liang, Systematic analyses identify the anti-fibrotic role of IncRNA TP53TG1 in IPF. Cell Death Dis. 13, 525 (2022). doi:10.1038/s41419-022-04975-7 Medline
- 83. K. J. Kurppa, Y. Liu, C. To, T. Zhang, M. Fan, A. Vajdi, E. H. Knelson, Y. Xie, K. Lim, P. Cejas, A. Portell, P. H. Lizotte, S. B. Ficarro, S. Li, T. Chen, H. M. Haikala, H. Wang, M. Bahcall, Y. Gao, S. Shalhout, S. Boettcher, B. H. Shin, T. Thai, M. K. Wilkens, M. L. Tillgren, M. Mushajiang, M. Xu, J. Choi, A. A. Bertram, B. L. Ebert, R. Beroukhim, P. Bandopadhayay, M. M. Awad, P. C. Gokhale, P. T. Kirschmeier, J. A. Marto, F. D. Camargo, R. Haq, C. P. Paweletz, K.-K. Wong, D. A. Barbie, H. W. Long, N. S. Gray, P. A. Jänne, Treatment-induced tumor dormancy through YAPmediated transcriptional reprogramming of the apoptotic pathway. Cancer Cell 37, 104-122.e12 (2020). doi:10.1016/j.ccell.2019.12.006 Medline
- 84. V. F. Fiore, M. Krajnc, F. G. Quiroz, J. Levorse, H. A. Pasolli, S. Y. Shvartsman, E. Fuchs, Mechanics of a multilayer epithelium instruct tumour architecture and function. Nature 585, 433-439 (2020). doi:10.1038/s41586-020-2695-9
- 85. M. J. Paszek, N. Zahir, K. R. Johnson, J. N. Lakins, G. I. Rozenberg, A. Gefen, C. A. Reinhart-King, S. S. Margulies, M. Dembo, D. Boettiger, D. A. Hammer, V. M. Weaver, Tensional homeostasis and the malignant phenotype. Cancer Cell 8, 241-254 (2005). doi:10.1016/j.ccr.2005.08.010 Medline
- 86. J. Herrera, C. A. Henke, P. B. Bitterman, Extracellular matrix as a driver of progressive fibrosis. J. Clin. Invest. 128, 45-53 (2018). doi:10.1172/JCI93557

Medline

- 87. J. D. Humphrey, E. R. Dufresne, M. A. Schwartz, Mechanotransduction and extracellular matrix homeostasis. Nat. Rev. Mol. Cell Biol. 15, 802-812 (2014). doi:10.1038/nrm3896 Medline
- 88. T. Ritterhoff, H. Das, G. Hofhaus, R. R. Schröder, A. Flotho, F. Melchior, The RanBP2/RanGAP1*SUM01/Ubc9 SUM0 E3 ligase is a disassembly machine for Crm1-dependent nuclear export complexes. Nat. Commun. 7, 11482 (2016). doi:10.1038/ncomms11482 Medline
- 89. I. Andreu, I. Granero-Moya, N. R. Chahare, K. Clein, M. Molina-Jordán, A. E. M. Beedle, A. Elosegui-Artola, J. F. Abenza, L. Rossetti, X. Trepat, B. Raveh, P. Roca-Cusachs, Mechanical force application to the nucleus regulates nucleocytoplasmic transport. Nat. Cell Biol. 24, 896-905 (2022). doi:10.1038/s41556-022-00927-7 Medline
- 90. A. M. Bolger, M. Lohse, B. Usadel, Trimmomatic: A flexible trimmer for Illumina sequence data. **Bioinformatics** 30. 2114-2120 doi:10.1093/bioinformatics/btu170 Medline
- 91. A. Dobin, C. A. Davis, F. Schlesinger, J. Drenkow, C. Zaleski, S. Jha, P. Batut, M. Chaisson, T. R. Gingeras, STAR: Ultrafast universal RNA-seq aligner. Bioinformatics 29, 15–21 (2013). doi:10.1093/bioinformatics/bts635 Medline
- 92. Y. Liao, G. K. Smyth, W. Shi, featureCounts: An efficient general purpose program for assigning sequence reads to genomic features. Bioinformatics 30, 923–930 (2014). doi:10.1093/bioinformatics/btt656 Medline
- 93. M. D. Robinson, D. J. McCarthy, G. K. Smyth, edgeR: A Bioconductor package for differential expression analysis of digital gene expression data. Bioinformatics 26, 139-140 (2010). doi:10.1093/bioinformatics/btp616 Medline
- D. R. Powell, Degust: interactive RNA-seq analysis; https://doi.org/10.5281/zenodo.3258932
- 95. M. R. Corces, S. W. Cho, H. Y. Chang, W. J. Greenleaf, T. J. Montine, P. A. Khavari, A. Kundaje, V. I. Risca, L. A. Orloff, M. Kasowski, A. C. Carter, M. R. Mumbach, A. Kathiria, B. Wu, K. S. Montine, A. J. Rubin, A. T. Satpathy, S. Vesuna, N. A. Sinnott-Armstrong, P. G. Greenside, E. G. Hamilton, A. E. Trevino, Omni-ATAC-seq: Improved ATAC-seq protocol, Protocol Exchange (2017);https://dx.doi.org/10.1038/protex.2017.096.
- 96. FastQC: A quality control tool for high throughput sequence data (Babraham Bioinformatics, Babraham Institute, 2010); https://www.bioinformatics.babraham.ac.uk/projects/fastgc/
- 97. B. Langmead, Aligning short sequencing reads with Bowtie. Curr. Protoc. Bioinformatics Chapter 11, 7 (2010). doi:10.1002/0471250953.bi1107s32 Medline
- 98. A. R. Quinlan, BEDTools: The Swiss-army tool for genome feature analysis. Curr. **47**, Protoc. **Bioinformatics** 11.12.1-11.12.34 (2014).doi:10.1002/0471250953.bi1112s47 Medline
- 99. Y. Zhang, T. Liu, C. A. Meyer, J. Eeckhoute, D. S. Johnson, B. E. Bernstein, C. Nusbaum, R. M. Myers, M. Brown, W. Li, X. S. Liu, Model-based analysis of ChIP-Seq (MACS). Genome Biol. 9, R137 (2008). doi:10.1186/gb-2008-9-9-r137
- 100. M. I. Love, W. Huber, S. Anders, Moderated estimation of fold change and dispersion for RNA-seg data with DESeg2. Genome Biol. 15, 550 (2014). doi:10.1186/s13059-014-0550-8 Medline
- 101. G. Yu, L.-G. Wang, Q.-Y. He, ChIPseeker: An R/Bioconductor package for ChIP peak annotation, comparison and visualization. Bioinformatics 31, 2382-2383 . (2015). doi:10.1093/bioinformatics/btv145 Medline
- 102. F. Ramírez, F. Dündar, S. Diehl, B. A. Grüning, T. Manke, deepTools: A flexible platform for exploring deep-sequencing data. Nucleic Acids Res. 42, W187-W191 (2014). doi:10.1093/nar/gku365 Medline
- 103. S. Heinz, C. Benner, N. Spann, E. Bertolino, Y. C. Lin, P. Laslo, J. X. Cheng, C. Murre, H. Singh, C. K. Glass, Simple combinations of lineage-determining transcription factors prime cis-regulatory elements required for macrophage and B cell identities. Mol. Cell 38, 576-589 (2010). doi:10.1016/j.molcel.2010.05.004 Medline
- 104. X. Wei, Y. Xiang, D. T. Peters, C. Marius, T. Sun, R. Shan, J. Ou, X. Lin, F. Yue, W. Li, K. W. Southerland, Y. Diao, HiCAR is a robust and sensitive method to analyze open-chromatin-associated genome organization. Mol. Cell 82, 1225-1238.e6 (2022). doi:10.1016/i.molcel.2022.01.023 Medline
- 105. A. Kechin, U. Boyarskikh, A. Kel, M. Filipenko, cutPrimers: A new tool for accurate

First release: 25 September 2025

- cutting of primers from reads of targeted next generation sequencing. J. Comput. Biol. 24, 1138-1143 (2017). doi:10.1089/cmb.2017.0096 Medline
- 106. N. Abdennur, G. Fudenberg, I. M. Flyamer, A. A. Galitsyna, A. Goloborodko, M. Imakaev, S. V. Venev; Open2C, Pairtools: From sequencing data to chromosome contacts. PLOS Comput. Biol. 20. e1012164 (2024).doi:10.1371/journal.pcbi.1012164 Medline
- 107. I. Juric, M. Yu, A. Abnousi, R. Raviram, R. Fang, Y. Zhao, Y. Zhang, Y. Qiu, Y. Yang, Y. Li, B. Ren, M. Hu, MAPS: Model-based analysis of long-range chromatin interactions from PLAC-seg and HiChIP experiments. PLOS Comput. Biol. 15. e1006982 (2019). doi:10.1371/journal.pcbi.1006982 Medline
- 108. N. Abdennur, L. A. Mirny, Cooler: Scalable storage for Hi-C data and other genomically labeled arrays. Bioinformatics 36, 311–316 doi:10.1093/bioinformatics/btz540 Medline
- 109. N. C. Durand, M. S. Shamim, I. Machol, S. S. P. Rao, M. H. Huntley, E. S. Lander, E. L. Aiden, Juicer provides a one-click system for analyzing loop-resolution Hi-C experiments. Cell Syst. 3, 95–98 (2016). doi:10.1016/j.cels.2016.07.002 Medline
- 110. A. R. Quinlan, I. M. Hall, BEDTools: A flexible suite of utilities for comparing Bioinformatics 26. features. 841-842 doi:10.1093/bioinformatics/btq033 Medline
- 111. J. Tycko, M. Wainberg, G. K. Marinov, O. Ursu, G. T. Hess, B. K. Ego, A. Aradhana, A. Li, A. Truong, A. E. Trevino, K. Spees, D. Yao, I. M. Kaplow, P. G. Greenside, D. W. Morgens, D. H. Phanstiel, M. P. Snyder, L. Bintu, W. J. Greenleaf, A. Kundaje, M. C. Bassik, Mitigation of off-target toxicity in CRISPR-Cas9 screens for essential non-coding elements. Nat. Commun. 10, 4063 (2019). doi:10.1038/s41467-019-11955-7 Medline
- 112. M. A. Horlbeck, L. A. Gilbert, J. E. Villalta, B. Adamson, R. A. Pak, Y. Chen, A. P. Fields, C. Y. Park, J. E. Corn, M. Kampmann, J. S. Weissman, Compact and highly active next-generation libraries for CRISPR-mediated gene repression and activation. eLife 5, e19760 (2016). doi:10.7554/eLife.19760 Medline
- 113. M. E. Berginski, S. M. Gomez, The Focal Adhesion Analysis Server: A web tool for analyzing focal adhesion dynamics. F1000Res. 2, 68 doi:10.12688/f1000research.2-68.v1 Medline
- 114. D. Yao, J. Tycko, J. W. Oh, L. R. Bounds, S. J. Gosai, L. Lataniotis, A. Mackay-Smith, B. R. Doughty, I. Gabdank, H. Schmidt, T. Guerrero-Altamirano, K. Siklenka, K. Guo, A. D. White, I. Youngworth, K. Andreeva, X. Ren, A. Barrera, Y. Luo, G. G. Yardımcı, R. Tewhey, A. Kundaje, W. J. Greenleaf, P. C. Sabeti, C. Leslie, Y. Pritykin, J. E. Moore, M. A. Beer, C. A. Gersbach, T. E. Reddy, Y. Shen, J. M. Engreitz, M. C. Bassik, S. K. Reilly, The ENCODE4 Consortium, Multicenter integrated analysis of noncoding CRISPRi screens. Nat. Methods 21, 723-734 (2024). doi:10.1038/s41592-024-02216-7 Medline
- 115. K. Clement, H. Rees, M. C. Canver, J. M. Gehrke, R. Farouni, J. Y. Hsu, M. A. Cole, D. R. Liu, J. K. Joung, D. E. Bauer, L. Pinello, CRISPResso2 provides accurate and rapid genome editing sequence analysis. Nat. Biotechnol. 37, 224-226 (2019). doi:10.1038/s41587-019-0032-3 Medline
- 116. F. Muerdter, Ł. M. Boryń, A. R. Woodfin, C. Neumayr, M. Rath, M. A. Zabidi, M. Pagani, V. Haberle, T. Kazmar, R. R. Catarino, K. Schernhuber, C. D. Arnold, A. Stark, Resolving systematic errors in widely used enhancer activity assays in human cells. Nat. Methods 15, 141-149 (2018). doi:10.1038/nmeth.4534 Medline
- 117. K. R. Sanson, R. E. Hanna, M. Hegde, K. F. Donovan, C. Strand, M. E. Sullender, E. W. Vaimberg, A. Goodale, D. E. Root, F. Piccioni, J. G. Doench, Optimized libraries for CRISPR-Cas9 genetic screens with multiple modalities. Nat. Commun. 9, 5416 (2018). doi:10.1038/s41467-018-07901-8 Medline
- 118. M. G. Gordon, F. Inoue, B. Martin, M. Schubach, V. Agarwal, S. Whalen, S. Feng, J. Zhao, T. Ashuach, R. Ziffra, A. Kreimer, I. Georgakopoulos-Soares, N. Yosef, C. J. Ye, K. S. Pollard, J. Shendure, M. Kircher, N. Ahituv, lentiMPRA and MPRAflow for high-throughput functional characterization of gene regulatory elements. Nat. Protoc. 15, 2387–2412 (2020). doi:10.1038/s41596-020-0333-5 Medline
- 119. G. Finak, A. McDavid, M. Yajima, J. Deng, V. Gersuk, A. K. Shalek, C. K. Slichter, H. W. Miller, M. J. McElrath, M. Prlic, P. S. Linsley, R. Gottardo, MAST: A flexible statistical framework for assessing transcriptional changes and characterizing heterogeneity in single-cell RNA sequencing data. Genome Biol. 16, 278 (2015). doi:10.1186/s13059-015-0844-5 Medline
- 120. T. Stuart, A. Butler, P. Hoffman, C. Hafemeister, E. Papalexi, W. M. Mauck 3rd, Y. Hao, M. Stoeckius, P. Smibert, R. Satija, Comprehensive integration of single-cell data. Cell 177, 1888-1902.e21 (2019). doi:10.1016/j.cell.2019.05.031 Medline

- 121. H. Katsura, V. Sontake, A. Tata, Y. Kobayashi, C. E. Edwards, B. E. Heaton, A. Konkimalla, T. Asakura, Y. Mikami, E. J. Fritch, P. J. Lee, N. S. Heaton, R. C. Boucher, S. H. Randell, R. S. Baric, P. R. Tata, Human lung stem cell-based alveolospheres provide insights into SARS-CoV-2-mediated interferon responses and pneumocyte dysfunction. Cell Stem Cell 27, 890-904.e8 (2020). doi:10.1016/i.stem.2020.10.005 Medline
- 122. P. Kadur Lakshminarasimha Murthy, V. Sontake, A. Tata, Y. Kobayashi, L. Macadlo, K. Okuda, A. S. Conchola, S. Nakano, S. Gregory, L. A. Miller, J. R. Spence, J. F. Engelhardt, R. C. Boucher, J. R. Rock, S. H. Randell, P. R. Tata, Human distal lung maps and lineage hierarchies reveal a bipotent progenitor. Nature 604, 111-119 (2022). doi:10.1038/s41586-022-04541-3 Medline
- 123. L. Bounds, B. Cosgrove, A. Barrera de Madariaga, L. Song, C. K. Taylor, G. Crawford, C. Gersbach, Mechanosensitive genomic enhancers potentiate the cellular response to matrix stiffness [software], version 1, Zenodo (2025); https://doi.org/10.5281/zenodo.17008807
- 124. C. S. Chen, Mechanotransduction a field pulling together? J. Cell Sci. 121, 3285-3292 (2008). doi:10.1242/ics.023507 Medline
- 125. K. A. Beningo, K. Hamao, M. Dembo, Y.-L. Wang, H. Hosoya, Traction forces of fibroblasts are regulated by the Rho-dependent kinase but not by the myosin light chain kinase. Arch. Biochem. Biophys. 456, 224-231 doi:10.1016/i.abb.2006.09.025 Medline
- 126. M. Chrzanowska-Wodnicka, K. Burridge, Rho-stimulated contractility drives the formation of stress fibers and focal adhesions. J. Cell Biol. 133, 1403–1415 (1996). doi:10.1083/jcb.133.6.1403 Medline
- 127. Y.-C. Chang, P. Nalbant, J. Birkenfeld, Z.-F. Chang, G. M. Bokoch, GEF-H1 couples nocodazole-induced microtubule disassembly to cell contractility via RhoA. Mol. Biol. Cell 19, 2147-2153 (2008). doi:10.1091/mbc.e07-12-1269 Medline
- 128. P. M. Hall, J. T. Inman, R. M. Fulbright, T. T. Le, J. J. Brewer, G. Lambert, S. A. Darst, M. D. Wang, Polarity of the CRISPR roadblock to transcription. Nat. Struct. Mol. Biol. 29, 1217-1227 (2022). doi:10.1038/s41594-022-00864-x Medline
- 129. N. Krietenstein, S. Abraham, S. V. Venev, N. Abdennur, J. Gibcus, T. S. Hsieh, K. M. Parsi, L. Yang, R. Maehr, L. A. Mirny, J. Dekker, O. J. Rando, Ultrastructural details of mammalian chromosome architecture. Mol. Cell 78, 554-565.e7 (2020). doi:10.1016/j.molcel.2020.03.003 Medline
- 130. N. S. Benabdallah, I. Williamson, R. S. Illingworth, L. Kane, S. Boyle, D. Sengupta, G. R. Grimes, P. Therizols, W. A. Bickmore, Decreased enhancer-promoter proximity accompanying enhancer activation. Mol. Cell 76, 473-484.e7 (2019). doi:10.1016/i.molcel.2019.07.038 Medline
- 131. J. Lee, J. Beliakoff, Z. Sun, The novel PIAS-like protein hZimp10 is a transcriptional co-activator of the p53 tumor suppressor. Nucleic Acids Res. 35, 4523-4534 (2007). doi:10.1093/nar/gkm476 Medline
- 132. Z. Yan, Y. Zhou, Y. Yang, C. Zeng, P. Li, H. Tian, X. Tang, G. Zhang, Zinc finger protein 384 enhances colorectal cancer metastasis by upregulating MMP2. Oncol. Rep. 47, 49 (2022). doi:10.3892/or.2022.8260 Medline
- 133. K. Torrungruang, M. Alvarez, R. Shah, J. E. Onyia, S. J. Rhodes, J. P. Bidwell, DNA binding and gene activation properties of the Nmp4 nuclear matrix transcription factors. J. Biol. Chem. 277, 16153-16159 (2002). doi:10.1074/jbc.M107496200
- 134. Z. Fan, G. Tardif, D. Hum, N. Duval, J.-P. Pelletier, J. Martel-Pelletier, Hsp90ß and p130cas: Novel regulatory factors of MMP-13 expression in human osteoarthritic 976-982 chondrocytes. Ann. Rheum. Dis. 68. (2009).doi:10.1136/ard.2008.092288 Medline
- 135. G. Khemlina, S. Ikeda, R. Kurzrock, The biology of hepatocellular carcinoma: Implications for genomic and immune therapies. Mol. Cancer 16, 149 (2017). doi:10.1186/s12943-017-0712-x Medline
- 136. B. Zhao, X. Ye, J. Yu, L. Li, W. Li, S. Li, J. Yu, J. D. Lin, C.-Y. Wang, A. M. Chinnaiyan, Z.-C. Lai, K.-L. Guan, TEAD mediates YAP-dependent gene induction and growth control. Genes Dev. 22, 1962-1971 (2008). doi:10.1101/gad.1664408 Medline
- 137. C. Johne, D. Matenia, X.-Y. Li, T. Timm, K. Balusamy, E.-M. Mandelkow, Spred1 and TESK1—Two new interaction partners of the kinase MARKK/TAO1 that link the microtubule and actin cytoskeleton. Mol. Biol. Cell 19, 1391-1403 (2008). doi:10.1091/mbc.e07-07-0730 Medline
- 138. K. A. Akter, M. A. Mansour, T. Hyodo, T. Senga, FAM98A associates with DDX1-C14orf166-FAM98B in a novel complex involved in colorectal cancer progression. Int. J. Biochem. Cell Biol. 84, 1-13 (2017). doi:10.1016/j.biocel.2016.12.013

First release: 25 September 2025

- 139. K. L. Jeffrey, M. Camps, C. Rommel, C. R. Mackay, Targeting dual-specificity phosphatases: Manipulating MAP kinase signalling and immune responses. Nat. Rev. Drug Discov. 6, 391-403 (2007). doi:10.1038/nrd2289 Medline
- 140. J. E. Molineros, B. Singh, C. Terao, Y. Okada, J. Kaplan, B. McDaniel, S. Akizuki, C. Sun, C. F. Webb, L. L. Looger, S. K. Nath, Mechanistic characterization of RASGRP1 variants identifies an hnRNP-K-regulated transcriptional enhancer contributing to susceptibility. Front. 10, 1066 (2019).SLF Immunol. doi:10.3389/fimmu.2019.01066 Medline
- 141. X.-J. Zhou, S. K. Nath, Y.-Y. Qi, C. Sun, P. Hou, Y.-M. Zhang, J.-C. Lv, S.-F. Shi, L.-J. Liu, R. Chen, W. Yang, K. Z. He, Y. Li, H. Zhang, Novel identified associations of RGS1 and RASGRP1 variants in IgA Nephropathy. Sci. Rep. 6, 35781 (2016). doi:10.1038/srep35781 Medline
- 142. J. M. Balko, L. J. Schwarz, N. E. Bhola, R. Kurupi, P. Owens, T. W. Miller, H. Gómez, R. S. Cook, C. L. Arteaga, Activation of MAPK pathways due to DUSP4 loss promotes cancer stem cell-like phenotypes in basal-like breast cancer. Cancer Res. 73, 6346–6358 (2013). doi:10.1158/0008-5472.CAN-13-1385 Medline
- 143. W. Jang, T. Kim, J. S. Koo, S.-K. Kim, D.-S. Lim, Mechanical cue-induced YAP instructs Skp2-dependent cell cycle exit and oncogenic signaling. EMBO J. 36, 2510-2528 (2017). doi:10.15252/embi.201696089 Medline
- 144. E. Sollis, A. Mosaku, A. Abid, A. Buniello, M. Cerezo, L. Gil, T. Groza, O. Güneş, P. Hall, J. Hayhurst, A. Ibrahim, Y. Ji, S. John, E. Lewis, J. A. L. MacArthur, A. McMahon, D. Osumi-Sutherland, K. Panoutsopoulou, Z. Pendlington, S. Ramachandran, R. Stefancsik, J. Stewart, P. Whetzel, R. Wilson, L. Hindorff, F. Cunningham, S. A. Lambert, M. Inouye, H. Parkinson, L. W. Harris, The NHGRI-EBI GWAS Catalog: Knowledgebase and deposition resource. Nucleic Acids Res. 51, D977-D985 (2023). doi:10.1093/nar/gkac1010 Medline

ACKNOWLEDGMENTS

We thank the Duke Sequencing Core and the Duke Viral Vector Core for their help and guidance, and members of the Gersbach and Crawford Labs at Duke University who provided feedback throughout this project. We thank the BioRepository and Precision Pathology Center (BRPC), Research Support (SSCRS), and Duke Surgery for providing human tissues under Institutional Review Board oversight and Substrate Services Core. We also thank Ruhi Rai for help with genomics data visualization and Zachary Farino for their suggestions. Figure panels containing images of sequencing machines were created with BioRender.com. Funding: National Institutes of Health grant UM1HG009428 (CAG. GEC): National Institutes of Health grant UM1HG012053 (CAG. GEC): National Institutes of Health grant U01AI146356 (CAG); National Institutes of Health grant RM1HG011123 (CAG, GEC); National Institutes of Health grant R01MH125236 (GEC, CAG); National Institutes of Health grant R35GM156302 (BDH); National Institutes of Health grant R01HL146557 (PRT); National Institutes of Health grant R01HL160939 (PRT); National Institutes of Health grant R01HL153375 (PRT); National Institutes of Health PROSPER grant T32HL160494 (TW); National Science Foundation grant EFMA-1830957; Allen Distinguished Investigator Award from the Paul G. Allen Frontiers Group (CAG); Open Philanthropy (CAG); NSF-GRFP (NSF-GRFP DGE - 2139754) (LRB, CKT); Regeneration Next Postdoctoral Fellowship (BDC). Author contributions: Conceptualization: BDC, LRB, CAG, GEC, BDH; Methodology: BDC, LRB, CAG, GEC, BDH, AB; Investigation: BDC, LRB, CKT, AB, ALS, AJR, TS, AS, LS, TW, AT; Visualization: BDC, LRB, NI; Funding acquisition: CAG, GEC, BDH; Project administration: BDC, LRB, CAG, GEC, BDH; Supervision: CAG, GEC, BDH, YD, PRT; Writing – original draft: BDC, LRB, NI; Writing – review & editing: BDC, LRB, CKT, CAG, GEC, BDH. Competing interests: CAG is a co-founder of Tune Therapeutics and Locus Biosciences, and an advisor to Tune Therapeutics and Sarepta Therapeutics. BDC, LRB, BDH, GEC, and CAG are inventors on a patent application PCT/US2024/057925 held/submitted by Duke University and related to this work. BDC is an employee of Tune Therapeutics. LRB is an employee of Xaira Therapeutics. The remaining authors have no conflicts of interest to declare. Data and materials availability: Public datasets used in this study are provided in table S23. All datasets generated in this study are available through the NCBI Gene Expression Omnibus (GEO) under accession number GSE243765 and the NIH IGVF Data Portal (data.igvf.org) under reference file IGVFFI8553BTYV. All code used in this manuscript is available in the Zenodo

online repository (123). Addgene catalog numbers for plasmids used in this study are noted in the methods. All materials used in this study will be made available upon request. Detailed protocols are available at https://www.protocols.io/workspaces/gersbach-lab. License information: Copyright © 2025 the authors, some rights reserved; exclusive licensee American Association for the Advancement of Science. No claim to original US government works. https://www.science.org/about/science-licenses-journalarticle-reuse

SUPPLEMENTARY MATERIALS

science.org/doi/10.1126/science.adl1988

Supplementary Text Figs. S1 to S29 Tables S1 to S31 References (124-144) MDAR Reproducibility Checklist

Submitted 4 October 2023; resubmitted 6 December 2024 Accepted 1 September 2025 Published online 25 September 2025 10.1126/science.adl1988

science.org

Table 1. Healthy donors.

	····		
	Age	Cause of death	Smoking history
Donor 1	33	Unknown	No
Donor 2	63	Head trauma; gun- shot wound	No
Donor 3	33	Head trauma; gun- shot wound	No
Donor 4	33	Intracranial hemor- rhage	Yes

Table 2. IPF donors.

	Age	Gender	Smoking history
Donor 1	63	Female	Unknown
Donor 2	75	Male	Unknown
Donor 3	53	Female	Unknown
Donor 4	58.9	Female	Yes

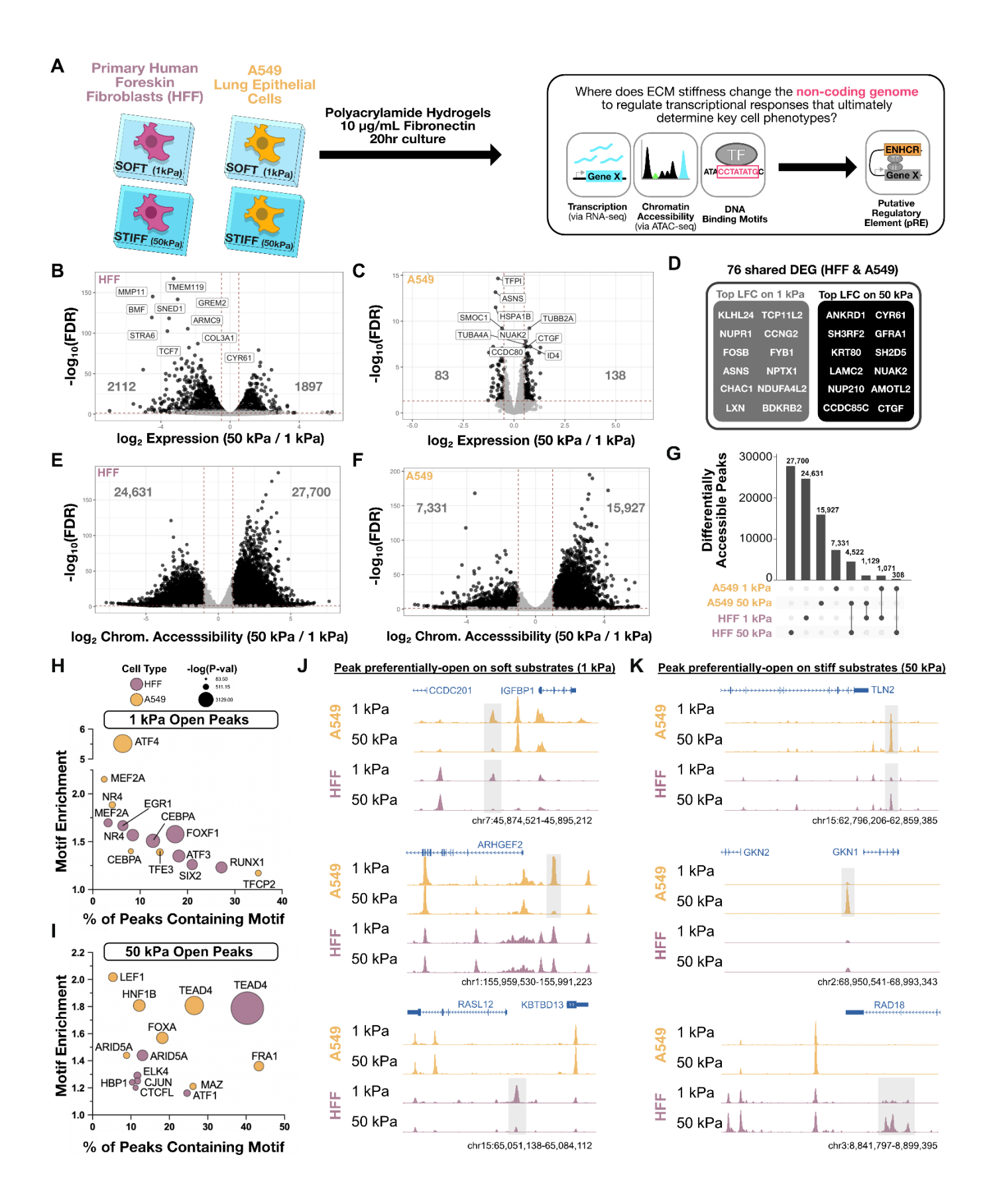


Fig. 1. Short-term culture on physiologically soft materials results in broad changes in gene expression and chromatin structure. (A) To assess how physiologically soft mechanical microenvironments affect the cellular epigenetic state, primary human neonatal foreskin fibroblasts (HFF cells) and A549 cells were cultured on soft (Elastic modulus, E=1kPa) or stiff (E= 50kPa) fibronectin-coated polyacrylamide hydrogels for 20 hours. (B to D) RNA-seq analysis revealed differentially expressed genes (FDR < 0.05, abs(Log2[Fold-Change])>0.5) in (B) HFF and (C) A459 cells, with overlapping differentially expressed genes shown in (D). (E to G) ATAC-seq analysis revealed differentially accessible chromatin regions (FDR < 0.01, abs(Log2 Fold-Change)>1) in HFF and A549 cells cultured on soft 1 kPa or stiff 50 kPa hydrogels [(E) and (F)], with overlap in accessibility between the two cell types displayed in (G). (H and I) ATAC-seq tracks showing representative regions with significantly higher accessibility (highlighted in grey) on soft 1 kPa hydrogels (e.g., near IGFBP1, ARHGEF2, RASL12) or on stiff 50 kPa hydrogels (e.g., near TLN2, GKN1, RAD18). The top two rows highlight peaks shared between both cell types, while the subsequent rows show cell type-specific peaks. (J and K) Transcription factor footprinting analysis using TOBIAS identified significantly enriched protein binding around key transcription factor motifs in differentially accessible regions on either 1 kPa or 50 kPa substrates in both HFF and A549 cells.

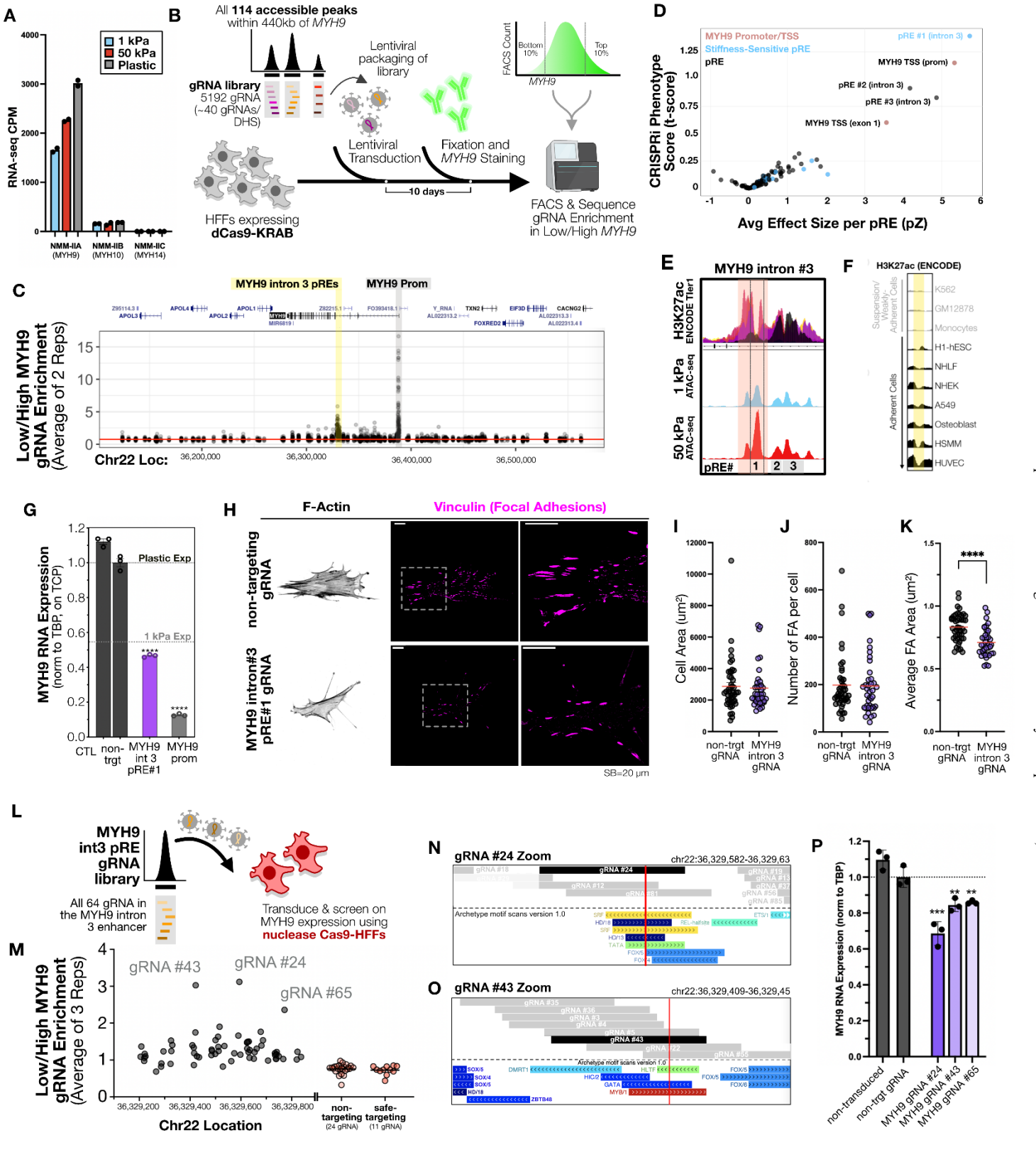


Fig. 2. CRISPRi screen reveals a mechanoenhancer in MYH9 intron 3 that regulates MYH9 expression and cell contractility. (A) RNA-seq data showing expression of MYH9 on soft 1 kPa hydrogels, stiff 50 kPa hydrogels, and TCP (N=2 reps/group). (B) Schematic of CRISPRi screening procedure for finding genomic regulators of MYH9 protein expression. (C) Individual gRNA enrichment in Low/High MYH9 expression bins following the MYH9 locus screen averaged across two replicates. (D) CRISPRi screening results across the MYH9 locus as shown by MYH9 Repression Phenotype Scores (t-score) and average effect size (z-score) as calculated for each DHS in the screen. Blue points indicate DHS was differentially accessible in ATAC-seq data between soft/stiff hydrogel conditions across both screen replicates. (E) ATAC-seq signal in the MYH9 intron 3 enhancer region, highlighting the forcesensitive pRE#1 subregion in yellow. (F) Normalized ENCODE H3K37ac signal around differentially accessible pRE#1 peak from MYH9 intron 3 region, compared across nine available ENCODE tier 1 cell lines. (G) Relative MYH9 RNA expression 10 days post-lentiviral transduction with dCas9KRAB and either a non-targeting gRNA, a MYH9 intron 3 enhancer-targeting gRNA, or an MYH9 promoter-targeting gRNA. The control (CTL) group represents cells without transduction. (H) Representative immunostaining images of F-actin and vinculin focal adhesions, with corresponding quantifications (I to K) of focal adhesion morphological parameters in HFF cells after transduction with either a non-targeting or a MYH9 intron 3 enhancer-targeting gRNA (N=39-45 FA/group, ** = p <0.01, **** = p<0.0001 by Student's t test). Red line indicates group means. (L) Schematic of Cas9 nuclease saturation indel screening performed across the MYH9 int3 enhancer region in HFF cells. (M) Results of the Cas9 screen, showing the ratio of gRNA enrichment in low vs. high MYH9 expression bins across the MYH9 intron 3 enhancer, compared to non-targeting gRNAs and ENCODE safe-targeting gRNAs. Data points represent averages across all three replicates. (N and O) gRNA positions of top hits relative to key motifs, including the core SRF CaRG motif (gRNA#24) and HLTF motif (gRNA#43). (P) Relative MYH9 expression in validation experiments for the top three gRNA hits from the screen, measured six days post-transduction (N=3 replicates/group).

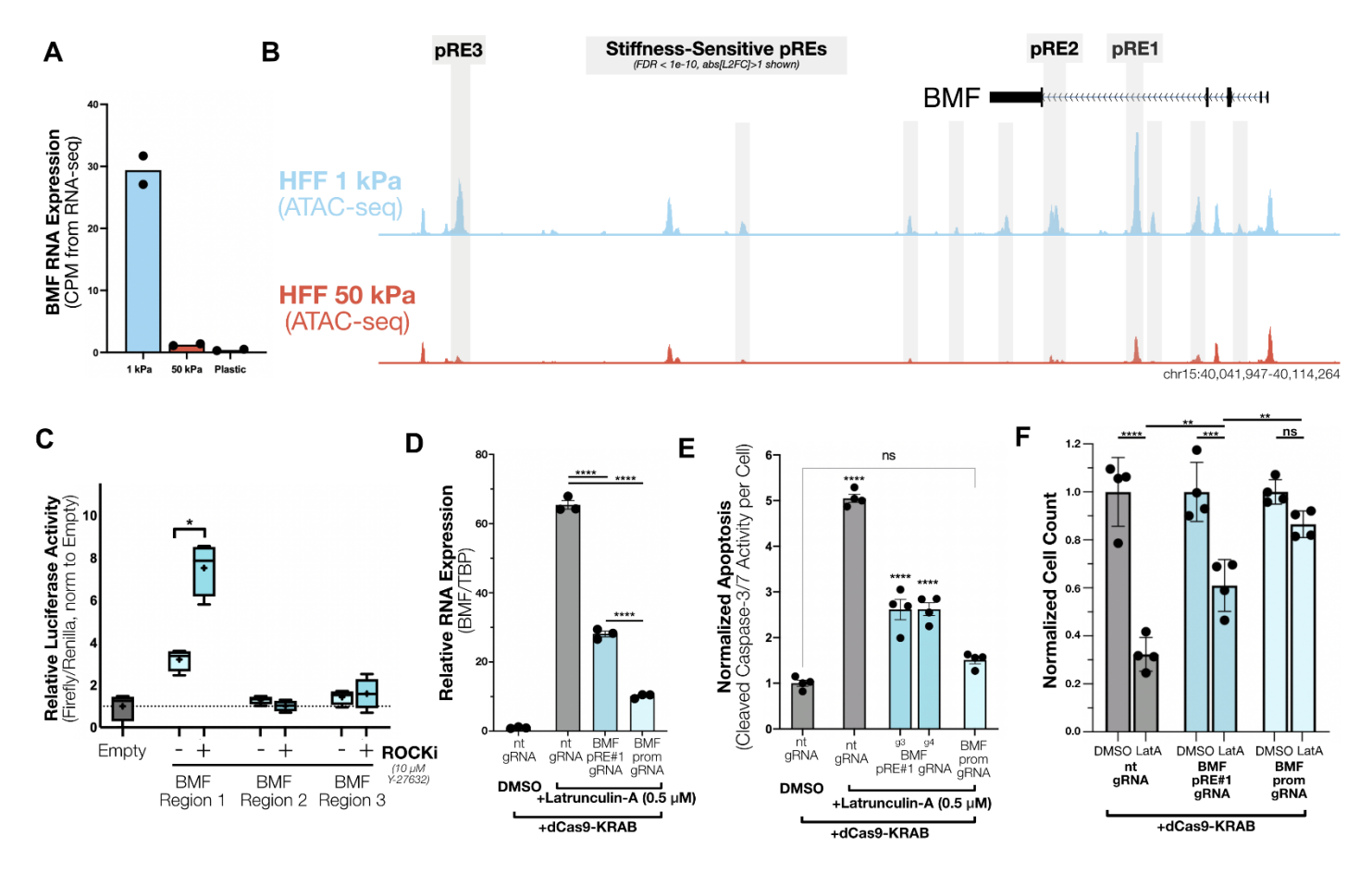


Fig. 3. BMF intron #4 mechanoenhancer has increased activity with reduced contractility and is a mediator of anoikis. (A) BMF RNA expression from RNA-seq in HFF cells cultured under different stiffness conditions (N=2 replicates per stiffness condition). (B) Comparison of ATAC-seq data for HFF cells grown on soft and stiff hydrogels. Grey highlights mark regions of differential chromatin accessibility between the stiffness conditions. (C) Luciferase enhancer reporter readouts from three of the BMF regions with and without 24 hours of 10 µM Y-27632 treatment, showing relative firefly luciferase activity controlled by these enhancers normalized to a control co-transfected renilla luciferase reporter. Box and whisker plots show median, plus indicates the group mean, and bars indicate the top/bottom 10% expression range (N=4 replicates/group). (D) Relative BMF RNA expression (N=3) and (E) normalized apoptosis as measured by Cleaved Caspase-3/7 activity (N=4 replicates/group) in HFF cells either untreated or transduced with various gRNAs following 24 hours of 0.5 µM Latrunculin-A ("LatA") treatment. (F) HFF cells transduced with dCas9-KRAB and either a non-targeting, BMF promoter, or BMF pRE#1 gRNA were seeded on TCP for one day in normal growth media, followed by treatment with either DMSO or 0.5 µM Latrunculin-A added to the media for an additional 72 hours. Following treatment, each HFF group was subjected to on-plate fixation followed by DAPI staining of cell nuclei and cell counting. All data shown was normalized to DMSO treated wells for each gRNA condition. All data are presented as mean ± SEM and are representative of at least two independent experiments. **** indicates p<0.0001, * indicates p<0.05 by Student's t test. Cleaved Caspase 3-7 activity and luciferase assay statistics are shown compared to the DMSO control group, while RNA expression comparisons are shown with overlay bars. "nt gRNA" refers to "non-targeting" gRNA.

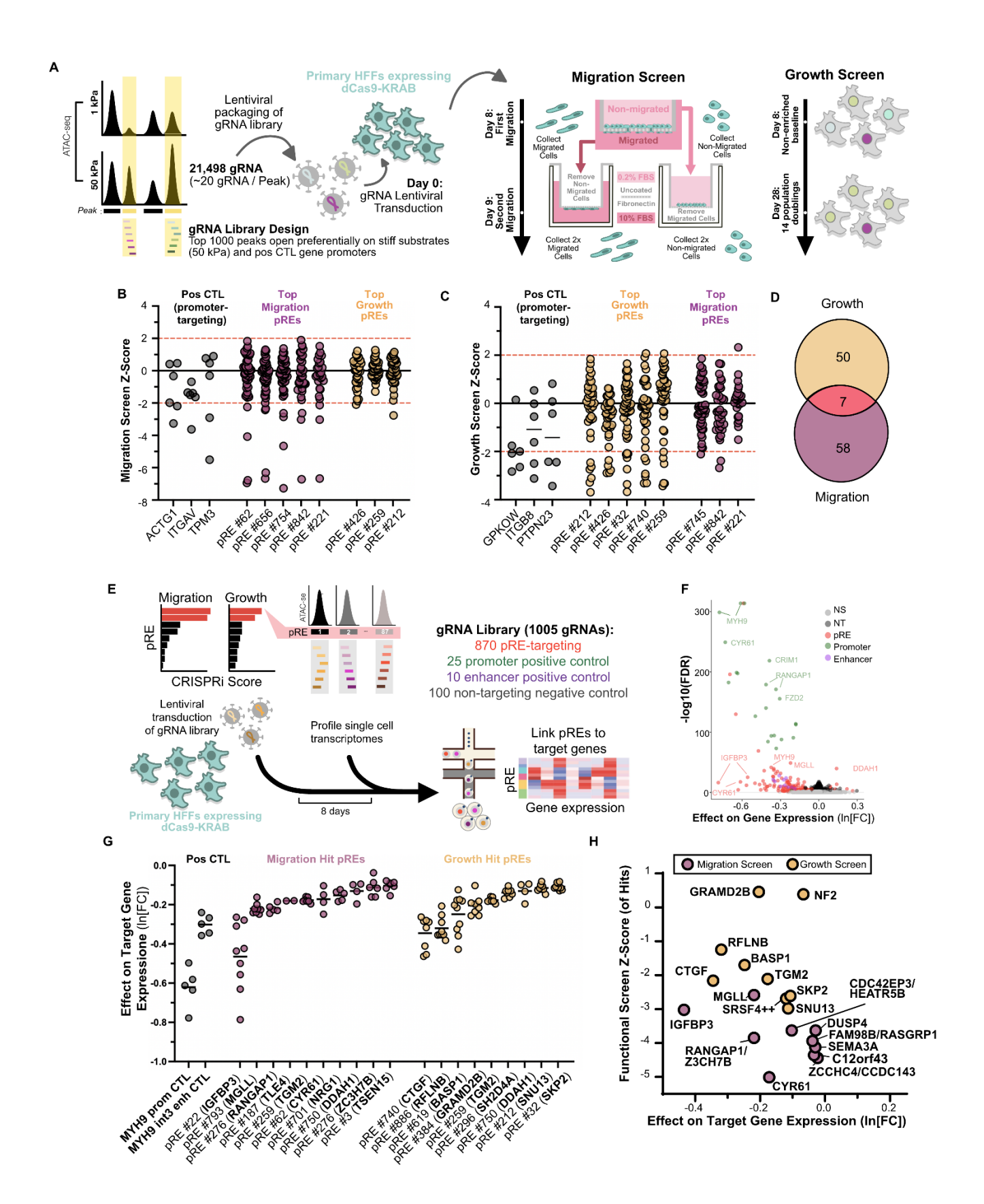


Fig. 4. Functional migration and growth screening paired with single cell CRISPRi screening identifies mechanosensitive regulatory elements driving functional behaviors and their target genes. (A) Schematic of the experimental setup for the paired migration and cellular growth screens in HFF cells, transduced with a CRISPRi library containing 21,498 gRNAs targeting the top 1,000 differentially accessible ATAC-seq peaks on stiff substrates. (B and C) Z-scores for migration (B) and growth (C) phenotypes, showing promoter positive controls, the top five pREs with the highest Z-scores for each phenotype, and three representative pREs ranked among the highest Z-scores for the other phenotype. Each dot represents a gRNA targeting a given pRE. Red dashed line indicates a Z-score threshold of two. (D) Venn diagram comparing the hit pREs regulating both phenotypes or only one. (E) Workflow overview of the single cell CRISPRi screen. A gRNA library targeting pREs identified from migration and growth screens was delivered to CRISPRi HFF cells, and single cell transcriptomes were profiled eight days later. (F) Volcano plot showing the change in target gene expression (InFC) versus significance [-log10(FDR)] for each gRNA-gene connection. Significant gRNA-gene connections are colored as follows:pRE ("NT," red), previously identified enhancers ("Enhancer," purple), promoter regions ("Promoter," green), and nontargeting controls ("NT," black), with an FDR < 0.01. Non-significant ("NS") gRNA-gene connections are shown in light grey. (G) Average effect on target gene expression for MYH9 promoter-targeting positive control gRNAs, intron 3 enhancer-targeting positive control gRNA (grey), and the top ten pREs affecting migration (yellow) and growth (purple). Points represent individual gRNA-gene linkages, with all regions showing significant target gene reduction (FDR < 0.01). (H) Z-scores of hit gRNAs for each pRE from functional screening plotted versus the average effect on target gene expression from the same pRE in the single cell screening. Points represent the top 10 pREs by Z-score from functional screening, along with the greatest absolute fold-change of pRE-gene linkages from the single cell RNA-seq screen.

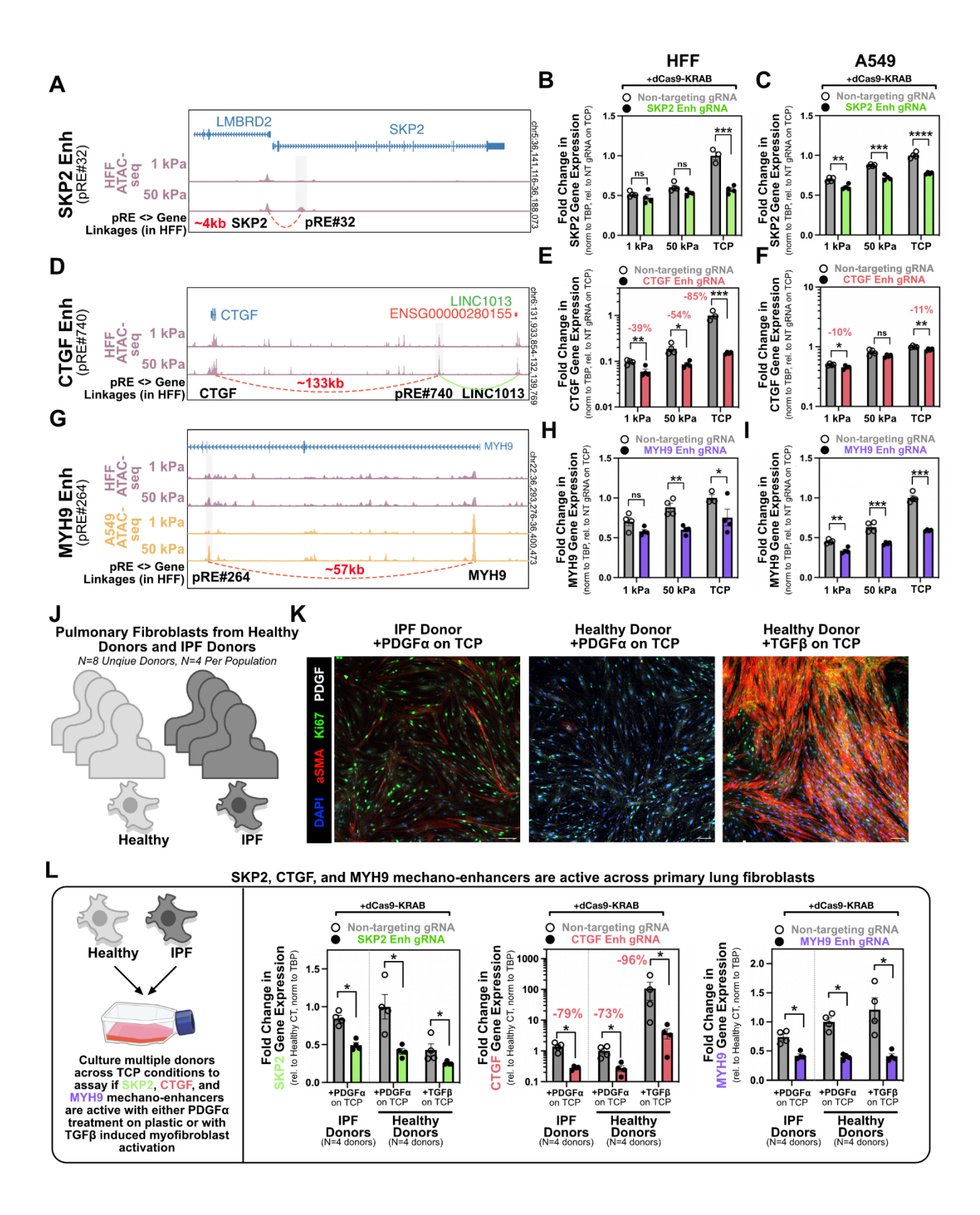


Fig. 5. Epigenetic repression of validated mechanoenhancers inhibits cellular mechano-responses across cell lines and pro-fibrotic disease contexts. (A) ATAC-seq and pRE-gene linkages in HFF cells showing SKP2 regulation by the mechanoenhancer at pRE#32. (B and C) Singleton validations of dCas9KRAB-induced mechanoenhancer SKP2 repression in (B) HFF cells and (C) A549 cells. (D) ATAC-seq and pRE-gene linkages in HFF cells showing regulation of CTGF and LINC1013 by the mechanoenhancer at pRE#740. (E and F) Singleton validations of dCas9KRAB-induced CTGF mechanoenhancer repression in (E) HFF cells, and (F) A549 cells, (G) ATAC-seq and pRE-gene linkages in HFF cells and A549 cells showing regulation of MYH9 by the mechanoenhancer at pRE#264. (H and I) Singleton validations of dCas9^{KRAB}-induced MYH9 mechanoenhancer repression across (H) HFF cells and (I) A549 cells. Each dot represents an independent biological replicate for HFF and A549 cells. (J) Lung fibroblasts were isolated from four healthy donors and four IPF patients. The baseline response of healthy donor cells (treated with PDGF α on TCP) was compared to IPF cells in the same conditions. Further, healthy donor cells were activated with TGFβ on TCP, and this response was compared to control baseline conditions. (K) Representative images show differences in α SMA staining under these conditions. (L) Singleton validations of dCas9KRAB-induced mechanoenhancer repression of the SKP2, CTGF, and MYH9 mechanoenhancers.